Petrogenesis of a Hybrid Cluster of Evolved Kimberlites and Ultramafic Lamprophyres in the Kuusamo Area, Finland

Hayden Dalton [1]*, Andrea Giuliani[1,2,†], Hugh O'Brien[3], David Phillips[1], Janet Hergt[1] and Roland Maas[1]

[1]KiDs (Kimberlites and Diamonds) Research Group, School of Earth Sciences, The University of Melbourne, Parkville, 3010 VIC, Australia; [2]Australian Research Council Centre of Excellence for Core to Crust Fluid Systems and GEMOC, Department of Earth and Planetary Sciences, Macquarie University, North Ryde, 2019 NSW, Australia; [3]Geological Survey of Finland, PO Box 96, Espoo, Finland

*Corresponding author. Telephone: +61 3 8344 7761. Fax: +61 3 8344 7675. E-mail: hayden.dalton@unimelb.edu.au
[†]Present address: Institute of Geochemistry and Petrology, Department of Earth Sciences, ETH Zurich

ABSTRACT

Kimberlites are often closely associated, both in time and space, with a wide variety of alkaline ultramafic rock types, yet the question of a genetic relationship between these rock types remains uncertain. One locality where these relationships can be studied within the same cluster is the Karelian craton in Finland. In this study we present the first petrographic, mineral and whole-rock geochemical results for the most recently discovered kimberlite cluster on this craton, which represents an example of the close spatial overlap of kimberlites with ultramafic lamprophyres. The Kuusamo cluster incorporates seven bodies [Kasma 45, Kasma 45 south, Kasma 47, Kalettomanpuro (KP), Kattaisenvaara (KV), Dike 15 and Lampi] distributed along a 60 km NE–SW corridor. Hypabyssal samples from KV, KP, Kasma 45 and Kasma 47 consist of altered olivine macrocrysts and microcrysts and phlogopite phenocrysts in a groundmass of perovskite, apatite, spinel, ilmenite, serpentine, and calcite. These petrographic features combined with mineral (e.g. Mg-rich ilmenite, Al–Ba-rich, Ti–Fe-poor mica) and whole-rock incompatible trace element compositions (La/Nb = 0·8 ± 0·1; Th/Nb = 0·07 ± 0·01; Nb/U = 66 ± 9) are consistent with these rocks being classified as archetypal kimberlites. These Kuusamo kimberlites are enriched in CaO and poor in MgO, which, combined with the absence of chromite and paucity of olivine macrocrysts and mantle-derived xenocrysts (including diamonds), suggests derivation from differentiated magmas after crystal fractionation. Samples from Lampi share similar petrographic features, but contain mica with compositions ranging from kimberlitic (Ba–Al-rich cores) to those more typical of orangeites–lamproites (increasing Si–Fe, decreasing Al–Ti–Ba), and have higher bulk-rock SiO_2 contents than the Kuusamo kimberlites. These features, combined with the occurrence of quartz and titanite in the groundmass, indicate derivation from a kimberlite magma that underwent considerable crustal contamination. This study shows that crustal contamination can modify kimberlites by introducing features typical of alkaline ultramafic rock types. Dike 15 represents a distinct carbonate-rich lithology dominated by phlogopite over olivine, with lesser amounts of titaniferous clinopyroxene and manganoan ilmenite. Phlogopite (Fe–Ti-rich) and spinel [high $Fe^{2+}/(Fe^{2+} + Mg)$] compositions are also distinct from the other Kuusamo intrusions. The petrographic and geochemical features of Dike 15 are typical of ultramafic lamprophyres, specifically, aillikites. Rb-Sr dating of phlogopite in Dike 15 yields an age of 1178·8 ± 4·1 Ma (2σ), which is considerably older than the ∼750 Ma emplacement age of the Kuusamo kimberlites. This new age indicates significant temporal overlap with the Lentiira–Kuhmo–Kostomuksha olivine lamproites emplaced ∼100 km to the SE. It is suggested that asthenospheric aillikite magmas similar to

Dike 15 evolved to compositions akin to the Karelian orangeites and olivine lamproites through interaction with and assimilation of MARID-like, enriched subcontinental lithospheric mantle. We conclude that the spatial coincidence of the Kuusamo kimberlites and Dike 15 is probably the result of exploitation of similar trans-lithospheric corridors.

INTRODUCTION

Although volumetrically insignificant globally, kimberlites have been emplaced on every continent with over 5000 known occurrences emplaced between 2·8 Ga and 12 ka (Tappe et al., 2018). These rocks have attracted considerable economic and scientific interest because they: (1) are the principal primary economic host rocks to diamonds at the Earth's surface; (2) are produced by some of the deepest derived magmas and, hence, provide a window into the Earth's mantle; and (3) entrain and transport to the surface a cargo of mantle xenoliths, which provide unique insights into the nature of the subcontinental lithosphere.

Kimberlites are rare, silica-poor, volatile-rich ($CO_2 \pm H_2O$), inequigranular igneous rocks. They typically form diatremes, which often contain several distinct units, as well as dikes and sills that may or may not be independent of the diatremes (e.g. Mitchell, 1986; Field et al., 2008; Scott Smith et al., 2013; Sparks, 2013). Kimberlites are 'hybrid' rocks consisting of a mixture of crustal and mantle xenocrysts and magmatic components. Apart from xenocrystic fragments, kimberlites are composed of macro- and microcrysts of olivine $\pm$ ilmenite and phlogopite, in a groundmass of olivine, spinel, perovskite, magnesian-ilmenite, phlogopite–kinoshitalite mica, apatite and monticellite, with a carbonate (calcite $\pm$ dolomite) and serpentine mesostasis (Mitchell, 1986, 2008).

Despite their significance and decades of study, the genesis of kimberlites remains enigmatic, as does the genetic relationship between kimberlites and other magma types. For example, some kimberlitic rocks overlap in space and/or time with carbonatites. These include occurrences in the Kola Alkaline Province, Russia (Beard et al., 1998; Downes et al., 2005), West Greenland–Labrador (e.g. Hutchison & Frei, 2009; Tappe et al., 2011, 2017b), mid-North America (Duke et al., 2014), the Deccan Large Igneous Province, India (Chalapathi Rao & Lehmann, 2011) and southern Africa (Dongre & Tappe, 2019). However, suggestions of a genetic link between these two lithologies remain contentious (e.g. Mitchell, 1979; Gaspar & Wyllie, 1984; Bell & Simonetti, 2010; Dongre & Tappe, 2019). Orangeites (previously known as Group II or 'micaceous' kimberlites), which are volatile-rich ($H_2O > CO_2$), olivine-rich, ultrapotassic rocks that also occur as diatremes and dike complexes, are often found associated with kimberlitic activity (e.g. Smith, 1983; Skinner, 1989; Mitchell, 1995). Examples of broadly coeval kimberlite and orangeite activity include Jurassic to Cretaceous magmatism in southern Africa (e.g. Smith et al., 1985; Le Roex, 1986; Skinner et al., 1994; Jelsma et al., 2009), Cambrian rocks in the Melville Peninsula of northern Canada (Sarkar et al., 2018), and (possibly) Devonian volcanism in the Arkhangelsk area of northwestern Russia (e.g. Beard et al., 2000; Mahotkin et al., 2000; Larionova et al., 2016). Kimberlites (and orangeites) may also be associated with ultramafic lamprophyres (UMLs), which represent a broad class of volatile-rich alkaline ultramafic rocks (e.g. Rock, 1991; Tappe et al., 2005). Kimberlites and UMLs that are closely associated in space and time are known from many areas worldwide, including the Yilgarn and Kimberley cratons (Western Australia) in the Paleoproterozoic (Fielding & Jaques, 1986; Graham et al., 2004), South Australia in the Jurassic (Scott-Smith et al., 1984), West Greenland in the Mesozoic and Neoproterozoic (e.g. Tappe et al., 2006, 2008, 2011, 2017b; Larsen et al., 2009; Nielsen et al., 2009; Secher et al., 2009), and the Devonian Kola Alkaline Province on the Terskii Coast (Fig. 1; e.g.; Beard et al., 1998; Downes et al., 2005). Kimberlites can also be associated with kamafugites, another alkaline mafic rock type, as is observed in the Cretaceous Alto Paranaiba Igneous Province of Brazil (e.g. Gibson et al., 1995; Guarino et al., 2013). Orangeites and kamafugites are typically ascribed to melting of metasomatized and/or veined lithospheric mantle in which veins may be composed of mica–amphibole–rutile–ilmenite–diopside (MARID) material (e.g. Mitchell, 1995; Foley et al., 2002; Tappe et al., 2008; Giuliani et al., 2015; Fitzpayne et al., 2018). However, in locations where this spectrum of magmas (including kimberlites) coexists, it has been argued that they may share a common asthenospheric source and that the resultant rock types at the surface are controlled by variable interaction with a heterogeneous lithospheric mantle (e.g. Chalapathi Rao & Lehmann, 2011; Tappe et al., 2011; Shaikh et al., 2018).

The Karelian craton, in northern Finland (Fig. 1), provides the opportunity to further explore possible relationships between kimberlites and other ultramafic lithologies. In this contribution, we document the petrography and mineral and bulk-rock chemistry of kimberlites and ultramafic lamprophyres from the Kuusamo Cluster. These results provide the first detailed information available for this cluster, which represents a relatively recent kimberlite discovery (see O'Brien & Bradley, 2008). Comparison of these new data with results available for worldwide kimberlites allows for a comprehensive classification of these
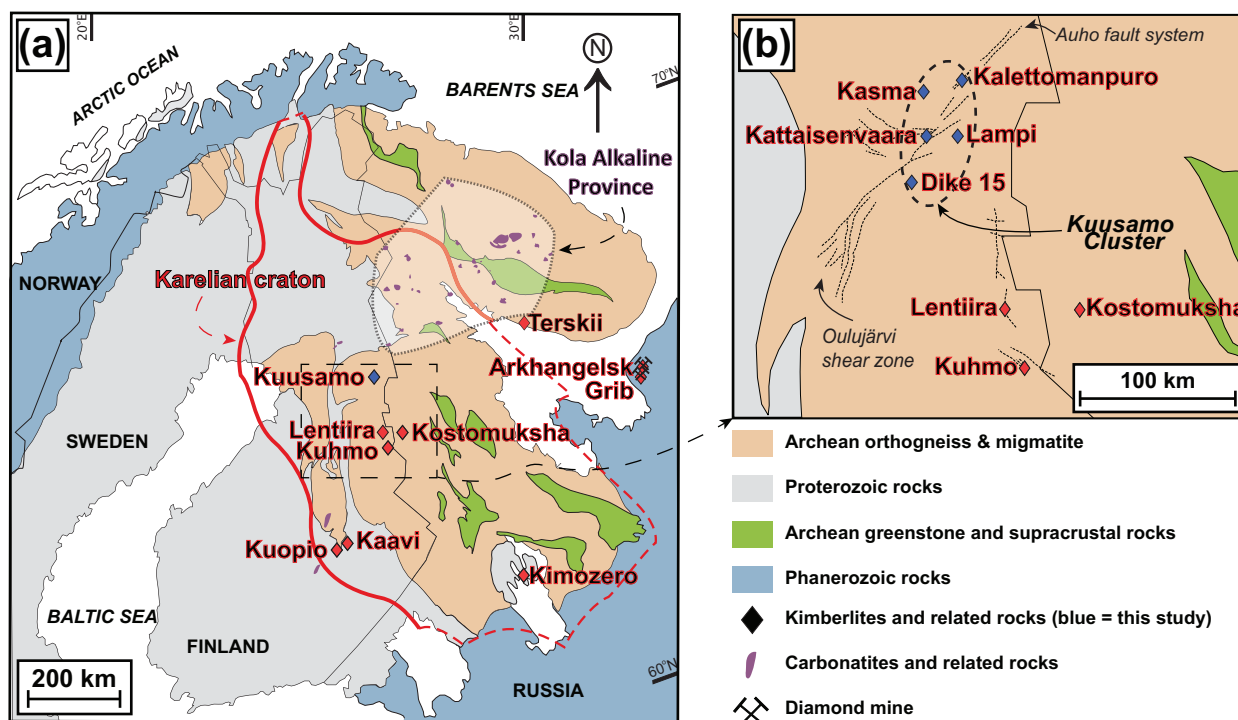
Fig. 1. (a) Geological map of the western Fennoscandian Shield. The red outline delimits the boundary of the Karelian craton. (b) Inset shows the distribution of bodies within the Kuusamo cluster that form the subject of this study. Major structural features are also shown (Laajoki, 2005). It should be noted that although Kasma is shown as a single site, two bodies from this locality are included in this investigation; modified from Lehtonen & O'Brien (2009) and Nironen (2017).

intrusions, as well as providing new insights into the petrogenesis of the contrasting lithologies. Despite 50 years of diamond exploration in Finland, research campaigns have not been directed at this region with the same intensity as has occurred in southern Africa or Canada, for example. Consequently, Finland is remarkably under-represented in the field of kimberlite studies and comparatively little is known about kimberlites and related rocks in this region (i.e. O'Brien & Tyni, 1999; O'Brien *et al.*, 2007; O'Brien, 2015; Dalton *et al.*, 2020). This contribution is the first attempt to bridge this gap.

GEOLOGICAL SETTING

Kimberlite and related magmatism in Finland is restricted to the Karelian craton. This craton is the nucleus of the Fennoscandian Shield, occupying ~400 000 km² —making it the largest of the Archean blocks in the region (Slabunov *et al.*, 2006; O'Brien & Lehtonen, 2012). The crust of the Karelian craton includes banded tonalite–trondhjemite–granodiorite (TTG) gneisses, and low-pressure greenstone and metasedimentary belts, which have been intruded by discrete plutons of granodioritic to monzo-granitic compositions. Higher-grade metasedimentary gneiss complexes are also present (Sorjonen-Ward & Luukkonen, 2005; Peltonen *et al.*, 2006).

Several occurrences of kimberlite and related alkaline ultramafic magmatism are known in Finland. The Kuhmo and Lentiira orangeites and olivine lamproites (Fig. 1) occur in a series of dikes focused along a north–south-trending fault zone in eastern Finland (O'Brien, 2015). On the Russian side of the Karelian craton and <50 km from Kuhmo–Lentiira (Fig. 1), more than 80 orangeite and olivine lamproite dikes and small breccia pipes have been identified in the Kostomuksha region (O'Brien *et al.*, 2007; Kargin *et al.*, 2014; O'Brien, 2015). These rocks were emplaced in the Mesoproterozoic between ~1232 and 1180 Ma based on phlogopite Rb–Sr and $^{40}Ar/^{39}Ar$ dating (Belyatskii *et al.*, 1997; O'Brien *et al.*, 2007; Phillips *et al.*, 2017b).

The most abundant kimberlite activity in Finland is represented by the two clusters that together form the Kaavi–Kuopio field (Fig. 1), which are located only 50 and 30 km inboard, respectively, from the southwestern margin of the Karelian craton. Twenty hypabyssal and volcaniclastic kimberlites have so far been discovered in this region (O'Brien & Tyni, 1999; Dalton *et al.*, 2020). The emplacement age of these bodies is poorly defined, with estimates ranging between ~434 and 626 Ma based on whole-rock K–Ar and perovskite U–Pb dating (O'Brien & Tyni, 1999; O'Brien *et al.*, 2005).

The Kuusamo cluster, which is the focus of the present study, is the most recently discovered kimberlite occurrence in Finland and consists of seven bodies [Kasma 45, Kasma 45 south, Kasma 47, Kalettomanpuro (KP), Kattaisenvaara (KV), Dike 15 and Lampi] distributed along a 60 km NE–SW corridor in the northern

Table 1: Details of samples used in this study

Pipe or dike and sample ID	Core depth (m)	Description	Mineralogy	Rock type
Kalettomanpuro	73·5	Dark grey, uniform, xenolith-poor, moderately olivine macrocrystic (up to 5 mm), inequigranular, coherent rock with prominent carbonate segregations and veins	Macrocrysts and microcrysts: olivine*, phlogopite–kinoshitalite	Coherent kimberlite (hypabyssal)
KP-01-04	93·5 96·9		Groundmass: phlogopite–kinoshitalite, spinel, apatite, Mg-ilmenite, perovskite, calcite, serpentine, monticellite*	
Kattaisenvaara	40·3	Dark grey, massive, xenolith-rich, weakly olivine macrocrystic (up to 5 mm), inequigranular, coherent rock	Macrocrysts and microcrysts: olivine*, phlogopite–kinoshitalite	Coherent kimberlite (hypabyssal)
KV001	61·4 61·7		Groundmass: phlogopite–kinoshitalite, spinel, apatite, Mg-ilmenite, perovskite, calcite, serpentine, monticellite*, (accessory: djerfisherite, Fe-sulphides)	
KV003	26·85 33·85	As above but light grey and more xenolith-rich		
Kasma 45	50·4	Light grey, massive, olivine macrocrystic (up to 3 mm) coherent rock	Macrocrysts and microcrysts: olivine*, phlogopite–kinoshitalite	Coherent kimberlite (hypabyssal)
KAS45-01			Groundmass: phlogopite–kinoshitalite, spinel, apatite, Mg-ilmenite, perovskite, calcite, serpentine, monticellite*	
KAS45-07	13·3	As above, more weakly olivine macrocrystic (up to 1 mm)		
Kasma 47	28·6	Dark grey–green, uniform, massive, xenolith-poor, oxide-rich, coherent rock	Microcrysts: phlogopite–kinoshitalite Groundmass: phlogopite–kinoshitalite, spinel, apatite, Mg-ilmenite, calcite, serpentine (accessory: Fe-sulphides)	Coherent kimberlite (hypabyssal)
KAS47-02	28·8	As above but inequigranular, olivine macrocryst-rich	As above with olivine*	
Lampi	72·8	Dark grey–green, massive, moderately xenolith-rich, olivine macrocrystic, coherent rock	Macrocrysts and microcrysts: olivine*, phlogopite–kinoshitalite	Coherent kimberlite (hypabyssal)
199-07	85·0		Groundmass: phlogopite–kinoshitalite, spinel, apatite, Mg-ilmenite, calcite, serpentine, monticellite*. (accessory: Fe-sulphides, titanite, quartz)	
Dike 15	30·67	Orange–brown, olivine and phlogopite macocrystic, coherent rock	Macrocrysts and microcrysts: olivine*, phlogopite	Ultramafic Lamprophyre
15.4	30·75		Groundmass: phlogopite, spinel, apatite, Mn-ilmenite, diopside, calcite, serpentine (accessory: Fe-sulphides)	

Descriptions follow the framework of Scott Smith *et al.* (2013).
*Denotes mineral phase that is now present as serpentinized or carbonatized pseudomorph.

portion of the Karelian craton (Fig. 1). Preliminary dating of samples from KV and KP provides discordant results: thermal ionization mass spectrometry (TIMS)-based perovskite U–Pb dating yielded ages of 756·8 ± 2·1 Ma and 759 ± 15 Ma for KV and KP, respectively (O'Brien & Bradley, 2008), whereas mica Rb–Sr and $^{40}Ar/^{39}Ar$ dating on a KP sample produced indistinguishable ages of 747 ± 4 Ma and 747·8 ± 1·0 Ma, respectively (Phillips *et al.*, 2017*b*).

Ultramafic lamprophyre (aillikite) dikes are also present in Finland, associated with the Devonian (365 ± 3 Ma) Sokli carbonatite complex (e.g. Vartiainen *et al.*, 1978; Kramm *et al.*, 1993; Lee *et al.*, 2003, 2005; O'Brien & Hyvönen, 2015). The Sokli complex is part of the Kola Alkaline Province (Fig. 1), which straddles the northern margin of the Karelian craton. Formation of the Kola Alkaline Province has been attributed to the impingement of a large mantle plume (Downes *et al.*, 2005).

SAMPLES

The samples used in this study were collected from drill-cores stored at the National Drill Core Archive of

the Geological Survey of Finland (GTK). The cores were largely extracted as part of 2004–2006 diamond exploration programs, by Sunrise Diamonds Plc. The 16 samples examined herein (Table 1) were selected on the basis of freshness from a larger set of 25 samples (0·1–0·5 kg) from Kasma 45, Kasma 47, KP, KV, Dike 15 and Lampi. Samples were not collected from Kasma 47 south owing to the highly friable nature of these rocks.

The detailed internal structure and morphology of all Kuusamo intrusions remains unknown and, therefore, limited geological context can be provided for the samples investigated. The KP and KV pipes are separated by 20 km and are both composed of intrusive coherent (hypabyssal) material. Hypabyssal material in the examined cores extends for up to 26 m and 42 m downhole, respectively (45° dip). The Lampi pipe, 15 km east of KV, includes more weathered hypabyssal material than at KP and KV, with a thickness of at least 40 m downhole (vertical drill hole). Brecciated volcaniclastic material was also recovered from Lampi and contains abundant sub-ovoid to angular altered crustal and/or mantle xenoliths (1–5 cm), which display strong reaction rims. This volcaniclastic material was not selected for the present study. Kasma 45 and 47, 20 km north of KV, are pipes

that extend for at least 60 m downhole (vertical drill hole) and consist of both hypabyssal and volcaniclastic material. The volcaniclastic hand specimens host abundant well-developed, ovoid, pelletal lapilli (1 cm; Supplementary Data Fig. S1; Supplementary Data are available for downloading at http://www.petrology.oxfordjournals.org) and angular fragments of country rock (1–2 cm). Because of their highly weathered nature, these volcaniclastic rocks were not included in this study. Hypabyssal material was sampled from Kasma 45. The samples from Kasma 47 derive from a discrete, 0·8 m thick interval of hypabyssal material that is sandwiched between volcaniclastic rock in the examined drill-core. This 'layer' of hypabyssal material could represent an unusually large autolith ($\sim$0·8 m) or a discrete intrusion. Dike 15 is located 20 km south of Lampi and KV and is 2 m wide with an estimated length of 1 km.

ANALYTICAL METHODS

Petrography
Textural and petrographic characterization was undertaken using a Leica DM750P petrographic microscope. Additional petrographic and mineral zonation observations were performed using a Philips (FEI) XL30 environmental scanning electron microscope (SEM), equipped with an OXFORD INCA energy-dispersive X-ray spectrometer (EDS), at the University of Melbourne. During the production of back-scattered electron (BSE) images and semi-quantitative chemical spot analysis, a beam acceleration voltage of 15 kV was employed.

Mineral chemistry
Major and minor oxide compositions of minerals were determined using a Cameca SX-50 and JEOL JXA-8530F electron probe micro analyser (EPMA) at the University of Melbourne (UoM) and a Cameca SX100 instrument at the Geological Survey of Finland, Espoo (GTK). Analytical conditions at UoM were as follows: beam acceleration voltage 15 kV, beam current $\sim$20 nA, beam diameter 1–8 μm (dependent on mineral phase; e.g. larger beam for mica), and counting times per analysis of 20 s on peak positions and 10 s on two background positions. The standards analysed for calibration purposes consisted of natural and synthetic materials [for full details see Fitzpayne *et al.*, 2018*b*)]. Operating conditions at GTK for silicates were 15 kV accelerating voltage, 20 nA sample current and 1–5 μm spot size. Oxides were analysed with 20 kV accelerating voltage, 40 nA sample current and 1 μm spot size. Natural minerals from the Astimex reference collection were used as standards. The PAP matrix correction software program was employed for all data reduction (Pouchou & Pichoir, 1984).

Whole-rock major and trace element compositions
Whole-rock powders for chemical analysis were prepared using an agate ball mill (Retsch Mixer Mill MM 400) from small ($<$5 mm) chips of kimberlite, after examination under a binocular microscope to select least altered and macroscopically xenolith-free kimberlite. Major elements were determined by fused disc X-ray fluorescence (XRF) spectrometry. Discs were prepared by fusing mixtures of rock powder ($\sim$0·6 g) and lithium borate flux (57 % tetraborate and 43 % metaborate; $\sim$4 g) at 1050 °C in an F-M4 (Initiative Scientific Products) bead casting machine. The discs were analysed on SPECTRO Xepos energy-dispersive XRF instruments at the University of Melbourne and University of Wollongong, using calibration lines based on certified reference materials. Results for quality control standards indicate that accuracy is $<$1–2 % for most elements, except for Na_2O (up to 4 %). Whole-rock CO_2 contents were determined at ALS (Vancouver) using photo-coulometry, which provides a lower limit of detection of 0·2 wt% CO_2.

Trace element concentrations were determined by solution-mode inductively coupled plasma mass spectrometry (ICP-MS) following Eggins *et al.* (1997) and Kamber *et al.* (2003). Whole-rock powder (0·075 g) was digested at high pressure using 3:1 HF–HNO_3 and 5M HNO_3 (further details see Supplementary Data). After dilution and addition of a multi-isotope spike, concentrations of 51 elements were determined on an Agilent 7700x quadrupole ICP-MS system at the University of Melbourne, using USGS standard W-2 (dolerite) as primary standard. Basalt standards BCR-2 (USGS) and BR (CRPG) analysed as unknowns yielded results that are consistent with long-term averages and reference values (Supplementary Data Table S7).

Rb–Sr geochronology of Dike 15
Rb–Sr dating of phlogopite was done following procedures adapted from Yaxley *et al.* (2013) and Maas *et al.* (2015). Splits of phlogopite grains ($>$0·5 mm, 6·5 and 16·4 mg) handpicked from Dike 15 were washed in hot distilled water (1 h), followed by dissolution of the smaller split in HF and HNO_3. The larger split was briefly leached with 2M HNO_3 (2 min, 20 °C) to remove calcite impurities, before dissolution of the residue in HF–HNO3. Using Rb–Sr concentration data obtained for small splits of the three fractions (bulk mica, acid-leached mica 'R', nitric acid leachate 'L'), ^{85}Rb–^{84}Sr spikes were added and equilibrated with the samples overnight. Sr and Rb were extracted and purified using Eichrom Sr resin and cation exchange columns. Procedural blanks ($<$0·1 ng) were negligible.

All isotopic analyses were done on a Nu Plasma multicollector (MC)-ICP-MS system. Kr and Rb concentrations were monitored for interference on Sr but were

below detection and no corrections were necessary. Strontium isotope ratios were internally normalized to $^{88}Sr/^{86}Sr = 8.37521$ as part of an online iterative spike stripping-normalization routine. $^{87}Sr/^{86}Sr$ are reported relative to $SRM987 = 0.710230$ and have an external precision (2σ) of ± 0.000040. Rb isotope dilution analyses were done using Zr-doping; $^{87}Rb/^{86}Sr$ determined by isotope dilution has an external precision of $\pm 0.5\%$ (2σ). The GLO-1 glauconite standard yields an Rb–Sr model age (assumed $^{87}Sr/^{86}Sr_i = 0.7074$) of 90.4 ± 0.6 Ma, consistent with the reference age of Odin (1982). Biotite from Mt Dromedary monzonite yields a 98.6 ± 0.6 Ma mineral isochron, consistent with $^{40}Ar-^{39}Ar$ ages (Phillips *et al.*, 2017*a*, and references therein). Rb–Sr ages were calculated using the ISOPLOT software of Ludwig (2003). The ^{87}Rb decay constant is $1.397 \times 10^{-11}\,a^{-1}$ (Villa *et al.*, 2015).

PETROGRAPHY

This section outlines thin-section scale petrographic details for the studied sample set, whereas hand specimen-scale descriptions are summarized in Table 1. Where samples display similar features to those already described, only the unique attributes for the sample are reported. All described samples are coherent, inequigranular rocks with altered euhedral olivine macro- and microcrysts. It is noteworthy that mantle-derived xenocrysts of garnet, clinopyroxene, orthopyroxene and chromite are absent in all the examined samples and macrocrystic ilmenite is only rarely observed in Kasma 45.

Kalettomanpuro
Three samples were examined from the Kalettomanpuro (KP) pipe. As is the case for all Kuusamo samples, olivine grains are completely pseudomorphed by carbonate and serpentine (Fig. 2a). About 40 vol% of the samples consist of altered olivine micro-phenocrysts (100–500 μm in maximum diameter), whereas olivine macrocrysts (1–10 mm) are less abundant. Both populations of relict olivine grains contain spinel inclusions in their rims.

Colourless phlogopite–kinoshitalite mica (100–200 μm) is prominent in carbonate-rich areas of the matrix and commonly exhibits a poikilitic texture. These euhedral, elongate oikocrysts contain chadacrysts of apatite, perovskite and spinel (Fig. 2b). Euhedral serpentine pseudomorphs are also poikilitically enclosed by mica, and their habit (euhedral to subhedral sub-equant tablets) is indicative of former monticellite grains. Zonation in mica is evident in BSE images (Fig. 2b; Supplementary Data Fig. S2a) and is defined by enrichment in Ba at grain margins, similar to mica in kimberlites elsewhere (e.g. Mitchell, 1986; Reguir *et al.*, 2009; Tappe *et al.*, 2014; Giuliani *et al.*, 2016).

Perovskite is abundant in the groundmass and occurs as euhedral grains (40–130 μm diameter) that exhibit clear zonation from darker cores to lighter rims (Supplementary Data Fig. S2b). Perovskite is often closely associated and occasionally intergrown with Magnesio-Ulvöspinel–Magnetite (MUM) spinel (Supplementary Data Fig. S2b). Spinel is present in the groundmass as anhedral to subhedral grains (30–80 μm), some with poorly developed 'atoll' textures. The 'lagoon' between the MUM core and magnetite rim is infilled by CaFeTi-silicates, probably schorlomite or other Ti-rich hydrogarnets, as also observed by Roeder & Schulze (2008) in kimberlites worldwide. Ti-magnetite is present as partially resorbed, anhedral macrocrysts that are zoned outwards towards increasing Mg, Al and Ti (>500 μm; Supplementary Data Fig. S3a). Magnesian ilmenite is another oxide phase present in the groundmass of KP as anhedral grains (30–70 μm). Ilmenite is notably less abundant than spinel and commonly appears as 'exsolution-like' lamellae within spinel (Supplementary Data Fig. S4a). Apatite is disseminated throughout the groundmass of KP, occurring in two textural habits; euhedral to subhedral tablets (40–50 μm) and acicular elongate needles (100–120 μm in their longest dimension). Monticellite replaced by serpentine is common in the groundmass (Supplementary Data Fig. S2a). The mesostasis consists of a mixture of calcite and serpentine, which is a feature common to the majority of Kuusamo samples in this study. In addition, large (i.e. >500 μm) segregations are dominated by calcite, but contain lesser apatite and mica, which is common to kimberlites worldwide (e.g. Armstrong *et al.*, 2004; Giuliani *et al.*, 2017; Castillo-Oliver *et al.*, 2018).

Kattaisenvaara
Samples from KV ($n = 5$) exhibit a similar texture and mineralogical composition to KP samples (Fig. 2c).

Mica is more abundant, and can reach a larger size (up to 1·3 mm) than in KP. Some KV mica grains display reverse zonation compared with that for KP, with Ba-rich cores (Supplementary Data Fig. S5a), and some oscillatory zoning is occasionally observed (Fig. 2d). However, most grains adhere to the 'kimberlitic' pattern of rimward Ba enrichment (e.g. Mitchell, 1986; Reguir *et al.*, 2009). Rare, tetraferriphlogopite rims are observed on some KV micas. Phlogopite is also present in KV samples as apparently late-stage anhedral, Ba-rich infillings with concentrically zoned margins (Supplementary Data Fig. S5b).

Groundmass perovskite (40–120 μm) from KV is unique for the Kuusamo rocks owing to the presence of subtle, oscillatory zoning (Supplementary Data Fig. S5c). In some instances, these zones appear partially resorbed. Perovskite also rarely develops glomeroporphyritic aggregates with spinel (Supplementary Data Fig. S5d). Compared with KP, perovskite grains exhibit more prominent incipient alteration at their edges, which are often replaced by titanite. Minor Fe-sulphides
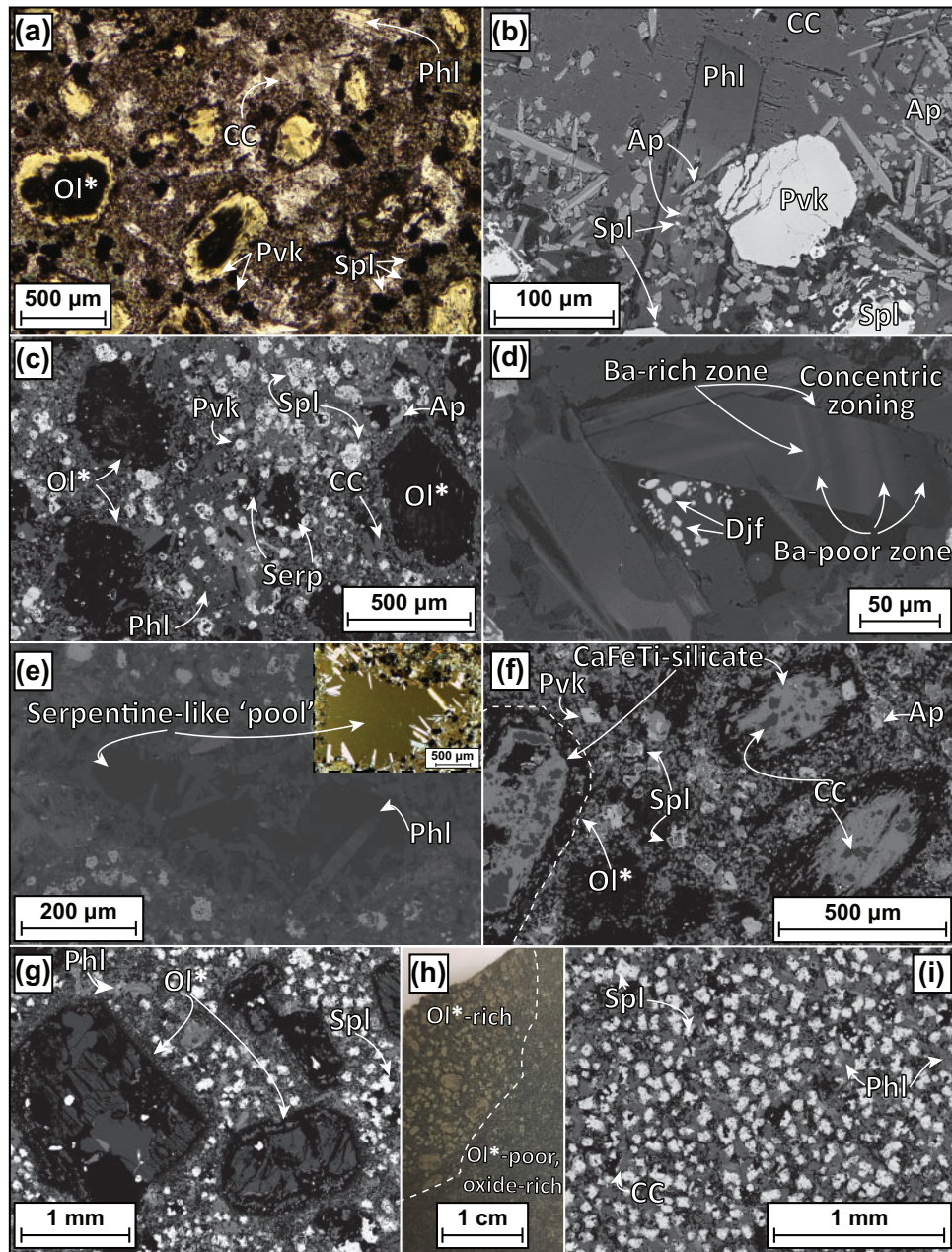
Fig. 2. Plane-polarized light photomicrograph (a, inset e), backscattered electron images (BSE) (b–g, i) and optical photograph (h) of select Kuusamo intrusions. Kalettomanpuro (KP): (a) inequigranular texture defined by micro-phenocrysts of serpentinized olivine (Ol) and smaller phlogopite (Phl), apatite (Ap), spinel (Spl) and perovskite (Pvk) set in a fine-grained mesostasis of serpentine and calcite (CC); (b) poikilitic phlogopite with inclusions of apatite, spinel and perovskite. Kattaisenvaara (KV): (c) inequigranular texture defined by micro-phenocrysts of serpentinized olivine and smaller groundmass phlogopite, apatite, spinel and perovskite set in a fine-grained mesostasis of serpentine (Serp) and calcite; (d) phlogopite with alternating Ba-rich and Ba-poor zones; the small djer-fisherite (Djf) sulphide grains should also be noted; (e) phlogopite laths radiating inward in a serpentine-like pool; this segregation is near isotropic in cross-polarized light (see Supplementary Data Fig. S5e-f). Kasma 45: (f) inequigranular texture defined by micro-phenocrysts of olivine replaced by CaFeTi-silicates and calcite; smaller groundmass constituents consist predominantly of apatite, spinel and perovskite. Kasma 47: (g) texture of 28·8 m sample dominated by relicts of olivine macrocrysts with a fine-grained groundmass of spinel, phlogopite and apatite; (h) hand-specimen displaying the difference between olivine-rich and olivine-poor–oxide-rich regions of Kasma 47; (i) texture of 28·6 m sample characterized by the absence of olivine relicts and an oxide-rich groundmass.

(40 μm) are present, as are rare, small, anhedral djer-fisherite grains.

Another unique feature of KV kimberlites is the presence of pale brown–yellow near-isotropic 'pools' with serpentine-like compositions (Fig. 2e). Similar

constituents have been described by Mitchell (2013) and as 'amygdale-like' by Exley & Jones (1983) in kimberlites from Canada (Ham West) and South Africa (De Beers dike), respectively. These segregations contain mica laths and coarse-grained calcite radiating into the

'pools' from the edges (Fig. 2e; Supplementary Data Fig. S5). However, the calcite phenocrysts (up to 700 μm in size; Supplementary Data Fig. S5e) are present both within discrete serpentine segregations and interspersed throughout the groundmass, and are a remarkable feature of these samples. Unlike KP, the mesostasis of KV is dominated by serpentine over carbonate.

Kasma 45

Olivine macrocrysts (2–4 mm) from Kasma 45 samples ($n = 2$) differ from the samples described above in that they are slightly more abundant and have been replaced by calcite and only minor serpentine (Fig. 2f; Supplementary Data S6a). In contrast, the dominant mode of alteration of the olivine microcrysts includes partial replacement by secondary hydrogarnets/CaFeTi-silicates in addition to calcite (Fig. 2f). These phases are similar to those described for replacement of spinel lagoons in KP and have also been observed replacing olivine in kimberlites from southern Africa and India (e.g. Stripp et al., 2006; Shaikh et al., 2017).

Phlogopite is both smaller (50–150 μm) and less abundant than for the previously described Kuusamo bodies and is zoned from Ba-poor cores to Ba-rich rims. Mica is also present as radial infillings in discrete phlogopite-rich segregations with interstitial serpentine (Supplementary Data Fig. S4d and e).

Euhedral to subhedral perovskite grains are more abundant in the groundmass (30–100 μm) than for any other rocks from the Kuusamo cluster. Perovskite is commonly associated with spinel and occurs in 'necklaces' around the rims of altered olivine. In some instances, perovskite appears to have grown around pre-existing groundmass magnesian ilmenite grains (<50 μm; Supplementary Data Fig. S6b). Rare examples of ilmenite macrocrysts are also present, although these too have been partially replaced by CaFeTi-silicates. The remaining groundmass and oxide population (Supplementary Data Figs S3c, S4b and S6b) is consistent with the KV and KP samples, with calcite being more abundant than serpentine.

Kasma 47

The two Kasma 47 samples differ by only 0·2 m depth of drill-core (Table 1), but display some notable petrographic differences. The sample from 28·6 m depth is devoid of olivine grains, or their alteration products, whereas the sample from 28·8 m hosts abundant altered olivine macrocrysts and lesser microcrysts (Fig. 2g–i). The contact between these olivine-rich and olivine-poor zones is sharp and distinct (Fig. 2h).

Both samples are rich in blocky, euhedral to anhedral, oxide or opaque phases, with the sample from 28·6 m being more enriched in these phases (Fig. 2i). This oxide (± sulphide) 'cumulate-like' texture and hand-specimen scale layering (Fig. 2h) is somewhat analogous to that observed at the Benfontein and

Wesselton Water Tunnel kimberlite sills in South Africa (Dawson & Hawthorne, 1973; Shee et al., 1994; White et al., 2012; Abersteiner et al., 2019). The spinels exhibit moderately well-developed 'atoll' textures with some altered to titanite (Supplementary Data Fig. S7a). Anhedral to subhedral magnesian ilmenite microcrysts (up to 700 μm), which are frequently overgrown by spinel, are part of this opaque phase population (Supplementary Data Fig. S4c). Accumulations of Fe-sulphide (Supplementary Data Fig. S7b) are also relatively common in Kasma 47 samples, often as anhedral infillings (50–200 μm) and veins associated with carbonate (up to 2 mm in length).

Phlogopite microphenocrysts (100–250 μm) are prominent throughout both samples and exhibit chemical zoning with Ba enrichment in the rims (Supplementary Data Fig. S7b). Similar to Kasma 45, accumulations of radiating or decussate textured mica and calcite are present in Kasma 47; however, in this case the mica grains are considerably smaller (50 μm) and have been largely altered to chlorite.

In the groundmass of Kasma 47, perovskite has been entirely replaced by titanite and minor anatase; similar perovskite replacement has also been observed in kimberlites globally (Chakhmouradian & Mitchell, 2000). There are other, less common, occurrences of titanite where euhedral grains (~30 μm) are rimmed by Ti-magnetite (Supplementary Data Fig. S7c). Apatite is present as either 30–40 μm euhedral tablets or more acicular grains (50–60 μm). The interstices between the groundmass phases of Kasma 47 are infilled with both calcite and serpentine. The sample from 28·6 m also contains rhombohedral calcite phenocrysts (up to 100 μm) in the groundmass as well as cross-cutting late-stage carbonate veins (Supplementary Data Fig. S7d and e).

Lampi

The three samples from Lampi contain euhedral to subhedral pseudomorphed olivine macrocrysts and, more abundant, microcrysts (Fig. 3a).

Phlogopite mica is an equally common phase in these rocks, present as poikilitic micro-phenocrysts (commonly 200–500 μm). Micas commonly exhibit chemical zonation; however, these patterns contrast to those described previously for KP, KV, and Kasma 45 and 47. It is common for Lampi phlogopite grains to contain well-defined, euhedral, Ba-rich cores with inclusions of spinel, perovskite and altered monticellite (Fig. 3c). This is the reverse of that observed in mica from kimberlites (e.g. Mitchell, 1986; Reguir et al., 2009). Similar to Kasma 47, small (20–100 μm) accumulations of chloritized mica and interstitial serpentine are present throughout.

Perovskite grains (40–100 μm) have been variably altered to titanite and anatase (e.g. Chakhmouradian & Mitchell, 2000; Martins et al., 2014). Discrete grains of titanite, up to 100 μm in length, are also present, often
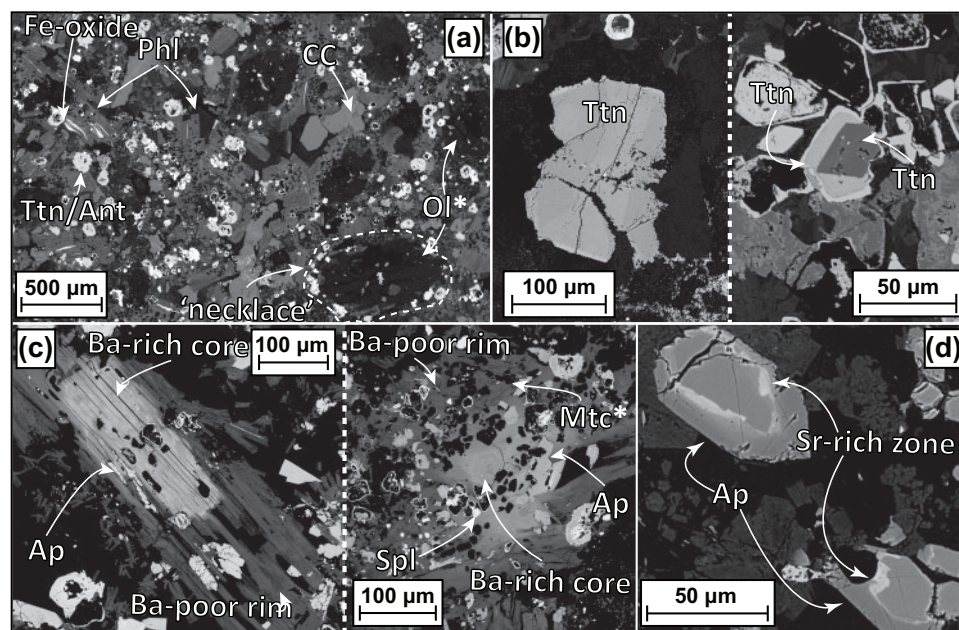
Fig. 3. Backscattered electron images of Lampi samples. (a) Rock texture, with olivine microphenocrysts well defined by 'necklaces' of spinel and altered perovskite grains. Phlogopite and calcite phenocrysts are also present in a groundmass of apatite, spinel and altered perovskite with a mesostasis of calcite and serpentine. (b) Examples of titanite (Ttn) (i.e. not replacing perovskite). The right-hand image shows a euhedral grain of titanite overgrown by spinel. (c) Variable forms of poikilitic phlogopite with Ba-rich cores hosting inclusions of apatite, spinel and altered monticellite (Mtc). (d) Euhedral to anhedral tablets of apatite exhibiting concentric zoning.

in calcite segregations. The titanite shape is not consistent with a perovskite pseudomorph and in some instances euhedral grains are rimmed by Ti-magnetite (Fig. 3b). In addition, anhedral, angular and partially resorbed grains of quartz (up to 70 μm) are scattered throughout the Lampi samples (Supplementary Data Fig. S8).

Other groundmass phases include Ti-magnetite (40–60 μm; Fig. 3d) and anhedral magnesian ilmenite (<5 vol%; up to 200 μm), which has been largely replaced by graphic intergrowths of rutile and Ti-magnetite (Supplementary Data Fig. S9). Apatite is common in the groundmass of Lampi rocks and can show zoning, including intermediate 'bright' (BSE imagery) Sr-rich regions (Fig. 3d). Apatite can also define elongated accumulations greater than 1 mm in length (Supplementary Data Fig. S10), which are commonly associated with phenocrysts of calcite (up to 500 μm). Calcite phenocrysts (up to 300 μm) are present throughout Lampi, although the mesostasis is dominated by serpentine over calcite.

Dike 15

Dike 15 samples (*n* = 2) are dominated by strongly pleochroic, orange–brown phlogopite phenocrysts (>1 mm in length). The larger grains are often complexly zoned with up to three distinct zones evident in transmitted light (Fig. 4b; Supplementary Data S11). The anhedral central zones are often resorbed and inclusion-free, in contrast to the inclusion-bearing zones surrounding

them. Phlogopite micro-phenocrysts and the rims of larger phenocrysts include spinel and altered perovskite. The poikilitic phlogopite phenocrysts in one sample (30·75 m) contrast with those from the sample recovered at 30·67 m, as they exhibit deformation textures including undulose extinction and kinked cleavages. Olivine is the other prominent phase in these rocks (micro-phenocrysts up to 500 μm and rare macrocrysts up to 2·5 mm), replaced invariably by serpentine and/or calcite (Fig. 4a).

The groundmass of Dike 15 includes partly altered grains of diopside (Fig. 4c and d); blocky, anhedral spinel (30–50 μm); elongate tablets of manganoan ilmenite (up to 100 μm; Fig. 4d); kassite ± titanite pseudomorphs after perovskite up to 100 μm in size; and rare iron-sulphides. Apatite was not observed in the sample from 30·75 m and, unlike the aforementioned intrusions, was a rare constituent of the groundmass in the sample from 30·67 m as anhedral grains ranging from 50 to 200 μm in size (Fig. 4d).

Calcite dominates the mesostasis, but is also present as discrete phenocrysts, including laths, up to 300 μm in length (Supplementary Data Fig. S12), enclosing oxide minerals and phlogopite.

MINERAL CHEMISTRY

The major and minor element compositions of mica, spinel, perovskite, apatite, ilmenite and clinopyroxene are reported in full in Supplementary Data Tables S1–6.
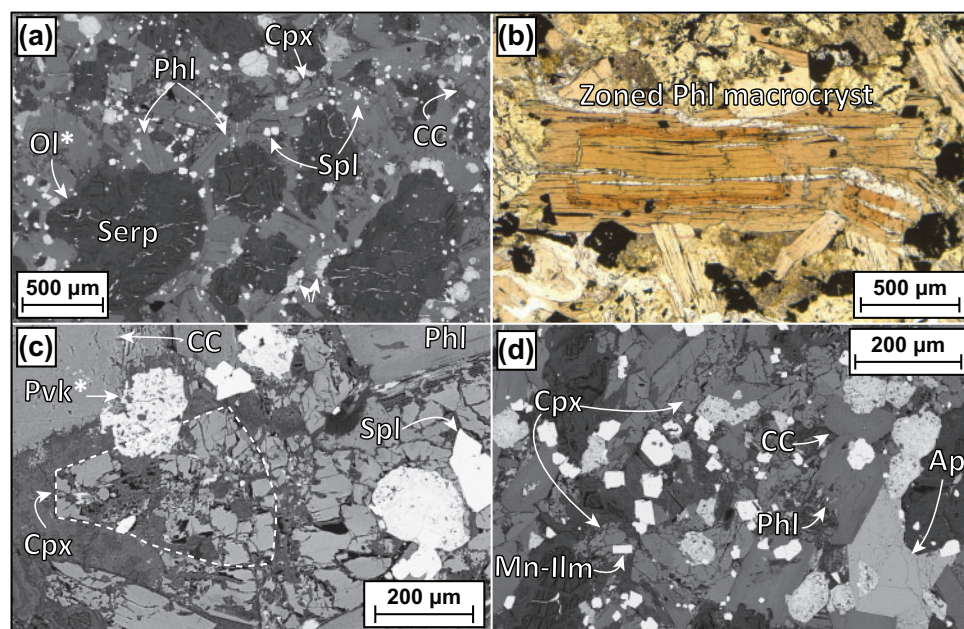
Fig. 4. Plane-polarized light photomicrograph (b) and backscattered electron images (a, c, d) of Dike 15 samples. (a) Rock texture with prominent phlogopite and serpentinized olivine microcrysts set in a mesostasis dominated by calcite. (b) Zoned phlogopite macrocryst with poikilitic overgrowths. (c) Detail of groundmass showing abundant clinopyroxene grains (Cpx) in Dike 15. (d) Detail of groundmass make-up including apatite, clinopyroxene, manganoan ilmenite (Mn-Ilm) and blocky spinel.

Mica

Mica compositions for KV, KP, Kasma 45, and Kasma 47 are Al- and Ba-rich kinoshitalite–phlogopite solid solutions (up to 10·1 wt% BaO, 20·8 wt% Al_2O_3, 0·1 wt% Cr_2O_3) and overlap with the compositional field of kimberlite groundmass micas (Fig. 5; e.g. Mitchell, 1995; Reguir *et al.*, 2009). Mica from these samples is commonly zoned with increasing BaO and Al_2O_3 from core to rim, with the variability best highlighted for mica from KV and KP (see also Fig. 2; Supplementary Data Figs S2 and S5). In some rare instances KV micas are mantled by tetraferriphlogopite (up to 9·9 wt% FeO). Kasma 47 mica trends towards higher Al_2O_3 and FeO than the other samples, and has slightly contrasting zonation, typically displaying decreasing TiO_2 and relatively constant FeO with increasing Al_2O_3 and BaO from cores to grain margins.

Where multiple samples were analysed from a single kimberlite intrusion, some mica compositions are distinct between samples. For example, average SiO_2, Al_2O_3 and BaO concentrations of mica from two different drill-cores of Kasma 45 differ by 6·2, 3·2 and 6·3 wt%, respectively. In addition, mica from two samples of KV, which are separated by 7 m in the same core, also show distinct BaO contents; up to 1·0 wt% in the 26·85 m sample, up to 9·1 wt% in the 33·85 m sample (Supplementary Data, Fig. S13).

Mica from Lampi is distinct from the other Kuusamo samples in that it is more enriched in FeO (3·5–6·8 wt%) and, locally, F (up to 2·8 wt%), but depleted in Al_2O_3 (8·8–14·4 wt%) at similar Ba concentrations (i.e. up to 11·1 wt% BaO; Fig. 5). The prominent zonation observed in Lampi is defined by a decrease in Al_2O_3, TiO_2, and BaO and concomitant increase in FeO, MgO and SiO_2 from core to rim. These compositions are somewhat transitional, extending from the field of kimberlitic mica to the tetraferriphlogopite compositions more commonly observed in orangeites, lamproites and aillikites (e.g. Mitchell, 1995; Tappe *et al.*, 2005), including the nearby Kuhmo–Lentiira–Kostomuksha cluster (Figs 1 and 5a, b). The elevated BaO contents are unusual for orangeite mica (typically well below 1 wt%; e.g. Mitchell, 1995); however, the evolution to Al-poor, Fe-rich mica compositions is consistent with the documented trend for orangeites (Fig. 5b).

Phlogopite from Dike 15 is enriched in FeO and TiO_2 compared with all other samples from the Kuusamo cluster (i.e. 6·6–10·2 wt% FeO, 1·6–7·6 wt% TiO_2, Fig. 5a–c), and lacks a Ba-kinoshitalite end-member component typical of kimberlitic micas (<3·3 wt% BaO, Fig. 5d). The composition of mica from Dike 15 overlaps those from ultramafic lamprophyres (Fig. 5a; see also Nielsen *et al.*, 2009; Tappe *et al.*, 2009). Analyses of inclusion-free, resorbed cores (Fig. 4; Supplementary Data Fig. S11) plot separately (Fig. 5a) and are characterized by elevated TiO_2 (7·5 ± 0·4 wt%) and Cr_2O_3 (1·0 ± 0·2 wt%) relative to inclusion-bearing phlogopite.

Spinel

A unique feature of Kuusamo spinel compositions is a general paucity of Cr-rich compositions (median 0·7 wt% Cr_2O_3) and the abundance of Ti-magnetite and magnetite. Indeed, the only Cr-rich compositions (up to 30·1 wt% Cr_2O_3) were observed in Lampi in two
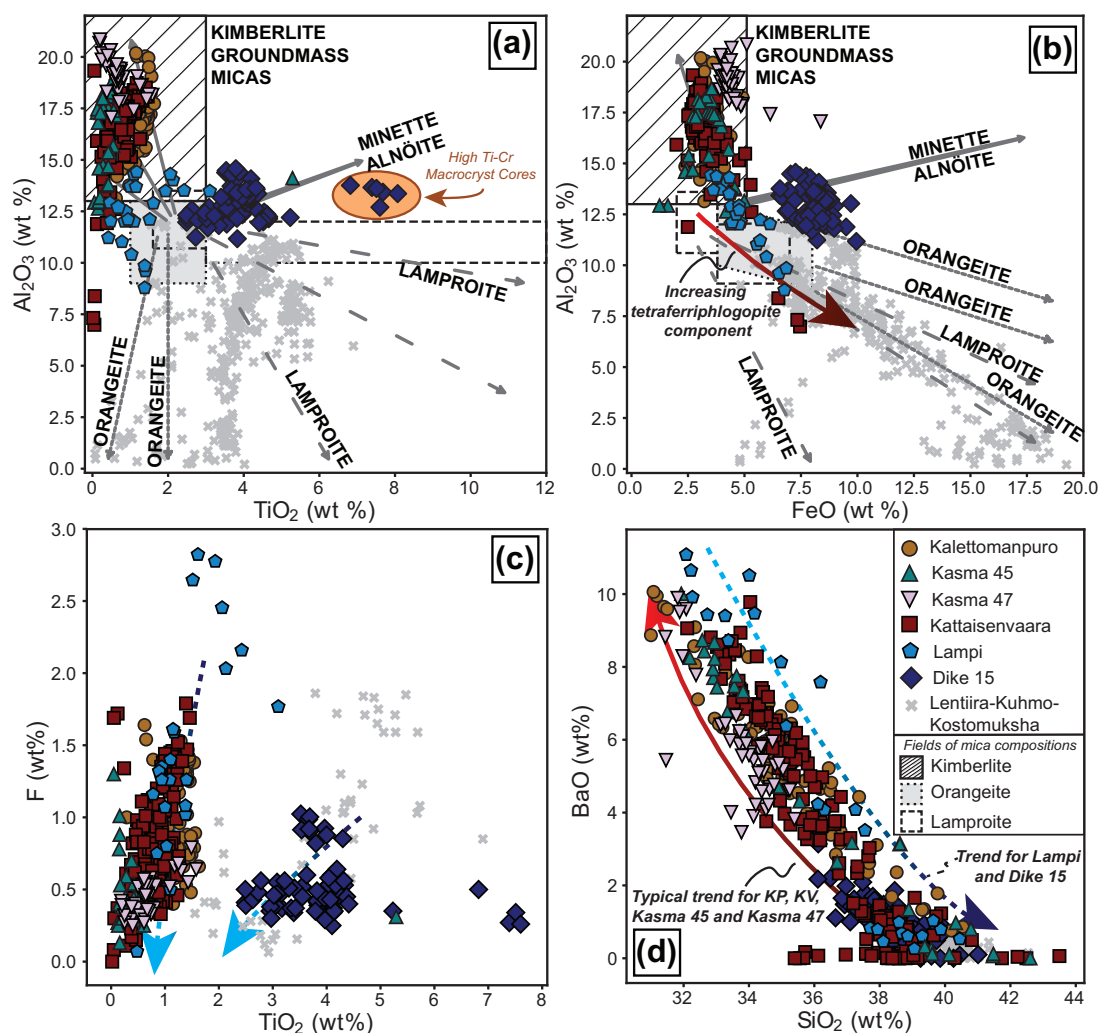
Fig. 5. (a) Al_2O_3 vs TiO_2, (b) Al_2O_3 vs FeO, (c) F vs TiO_2 and (d) BaO vs SiO_2 co-variation plots for mica in the Kuusamo rocks compared with mica compositions from the Lentiira–Kuhmo–Kostomuksha orangeite cluster [unpublished data combined with those from Kargin *et al.* (2014)]. Discrimination fields and evolutionary trends from Mitchell (1986, 1995). Arrows in (c) and (d) indicate variance in concentration of the element from core to rim of mica grains.

resorbed cores from a single spinel aggregate (Supplementary Data Fig. S15). Regardless, spinel from most samples (except for Kasma 47) exhibits a clear evolution from chromian-rich compositions to MUM compositions to magnetite. Spinels from Lampi, KV and KP are aligned with magmatic trend 1 (Fig. 6); that is, a trend of increasing Ti and Fe^{3+} and decreasing Cr, at near constant $Fe^{2+}/(Fe^{2+} + Mg)$, which is typical of spinel in kimberlites worldwide (Mitchell, 1986; Roeder & Schulze, 2008). The two KV samples that exhibit contrasting mica compositions (Supplementary Data Fig. S13) also have variable spinel compositions. The sample from 26·85 m is poorer in MgO (2·2 ± 1·4 vs 4·7 ± 0·7 wt%; *n* = 13 and 21, respectively) and richer in FeO (30·2 ± 1·3 vs 25·1 ± 1·5 wt%) than the sample from 33·85 m in the same drill-core (Supplementary Data Fig. S14). Spinel compositions from Kasma 45 and 47 are similar to those of trend 1, but plot at marginally higher

Fe^{2+}/Mg and show limited compositional evolution (especially Kasma 47; Fig. 6). In contrast, spinel from Dike 15 follows magmatic trend 2 (Fig. 6), defined by increasing Ti and Fe^{2+} with increasing $Fe^{2+}/(Fe^{2+} + Mg)$. This trend is typical of spinel in a range of ultramafic magmas including ultramafic lamprophyres (e.g. Rock, 1991; Tappe *et al.*, 2006). Spinel compositions from the nearby Lentiira–Kuhmo–Kostomuksha orangeite and olivine lamproite cluster are much more Cr-rich than those from Kuusamo.

Perovskite

Major element compositions of perovskite grains from Kasma 45, KV and KP are typical of kimberlitic perovskite (> 94 mol% $CaTiO_3$) with minor amounts of Nb_2O_5 (0·3–1·5 wt%), rare earth element (REE)-oxides (sum of Ce_2O_3 and Nd_2O_3; 1·0–3·2 wt%), Fe_2O_3 (0·7–1·7 wt%), and Na_2O (0·2–0·7 wt%; Fig. 7; Supplementary Data Fig.
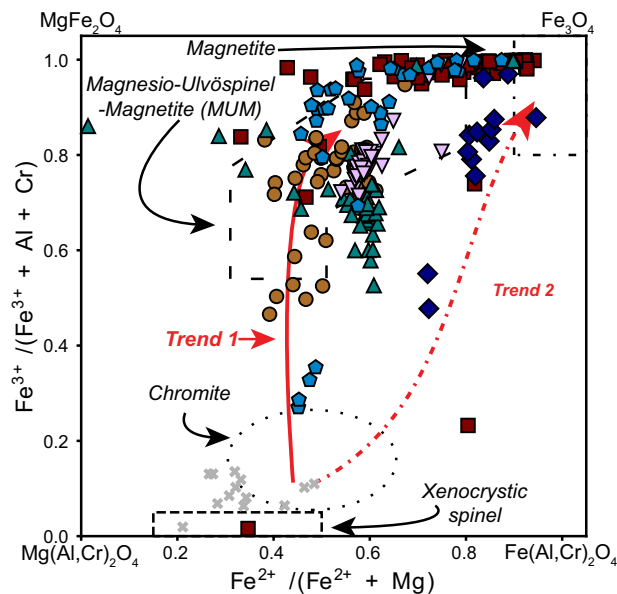
Fig. 6. $Fe^{3+}/(Fe^3 + Al + Cr)$ vs $Fe^{2+}/(Fe^{2+} + Mg)$ co-variation plot for spinel in the Kuusamo rocks compared with spinel compositions from the Lentiira–Kuhmo–Kostomuksha orangeite cluster [data from Kargin *et al.* (2014)]. Discrimination fields and magmatic evolution trend arrows from Roeder & Schulze (2008). Symbols and colours as for Fig. 5.

S16). Perovskite from KV is distinguished from KP and Kasma 45 by greater concentrations of Nb, Na and REE, resulting in compositions that extend further towards the loparite (up to 3·7 mol% $Na_{0.5}\Sigma REE_{0.5}TiO_3$) and lueshite (up to 1·6 mol% $NaNbO_3$) end-member compositions (Fig. 7). In comparison, perovskite from the Kostomuksha and Lentiira orangeites and olivine lamproites is significantly enriched in REE (Ce_2O_3 up to 6·4 wt%; Supplementary Data Fig. S16) and Sr (SrO up to 0·86 wt%; Kargin *et al.*, 2014), which is common to orangeitic perovskite observed elsewhere (e.g. Mitchell, 1995).

Ilmenite

Ilmenite grains from KV, KP, and Kasma 45 and 47 are all magnesian (up to 20·7 wt% MgO), with moderate Cr_2O_3 (up to 6·0 wt%) and low MnO contents (up to 2·0 wt%). Owing to alteration (Supplementary Data Fig. S9), only one grain could be analysed from Lampi, but its composition is similar to those of the other Kuusamo samples (16·6 wt% MgO, 5·3 wt% Cr_2O_3, 0·8 wt% MnO). These compositions are consistent with kimberlitic ilmenite (Fig. 8; e.g. Wyatt *et al.*, 2004). Ilmenite compositions from Dike 15 (MnO 7·3 ± 1·8 wt%; Cr_2O_3 0·5 ± 0·3 wt%; MgO 0·1 wt%) are unlike ilmenite in kimberlites owing to their elevated Mn and very low Mg concentrations (Fig. 8). Mn-ilmenite has been suggested to have a secondary origin in kimberlites, resulting from fluid metasomatism ('carbonatitic' or Mn-rich hydrothermal fluids; e.g. Castillo-Oliver *et al.*, 2017), but is more common as a primary magmatic phase in orangeites (e.g. Mitchell, 1995). Although published ilmenite
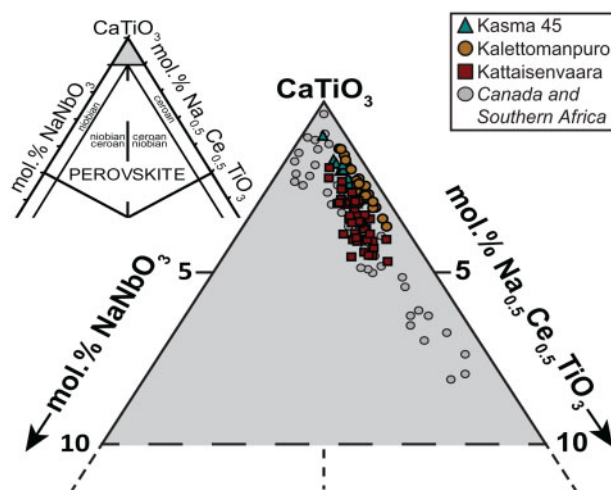

Fig. 7. Composition of perovskite cores from the Kuusamo rocks. Distinct groupings are evident for each of the three pipes shown. [Ternary proportions calculated using the method of Locock & Mitchell (2018); compositional fields and data for perovskites from Canada and Southern Africa from Chakhmouradian & Mitchell (2000).]
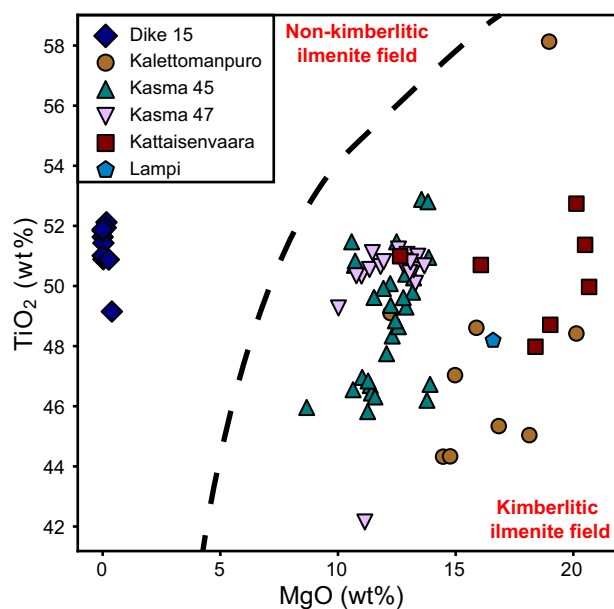

Fig. 8. TiO_2 vs MgO plot for ilmenite in the Kuusamo rocks; kimberlite and non-kimberlite discrimination fields from Wyatt *et al.* (2004).

data for UMLs are limited, they too exhibit elevated MnO contents (up to 11 wt%; e.g. Rock, 1986, 1987; Tappe *et al.*, 2004, 2006).

Apatite

Based on halogen site occupancy, the majority of apatites from Kuusamo intrusions are classified as fluorapatite (>0·5 a.p.f.u. F; up to 3·5 wt% F; Fig. 9d), with varying, subordinate, hydroxyl end-member components. Chlorine contents are below detection limit. A minority (<25%) of the analysed apatite grains from
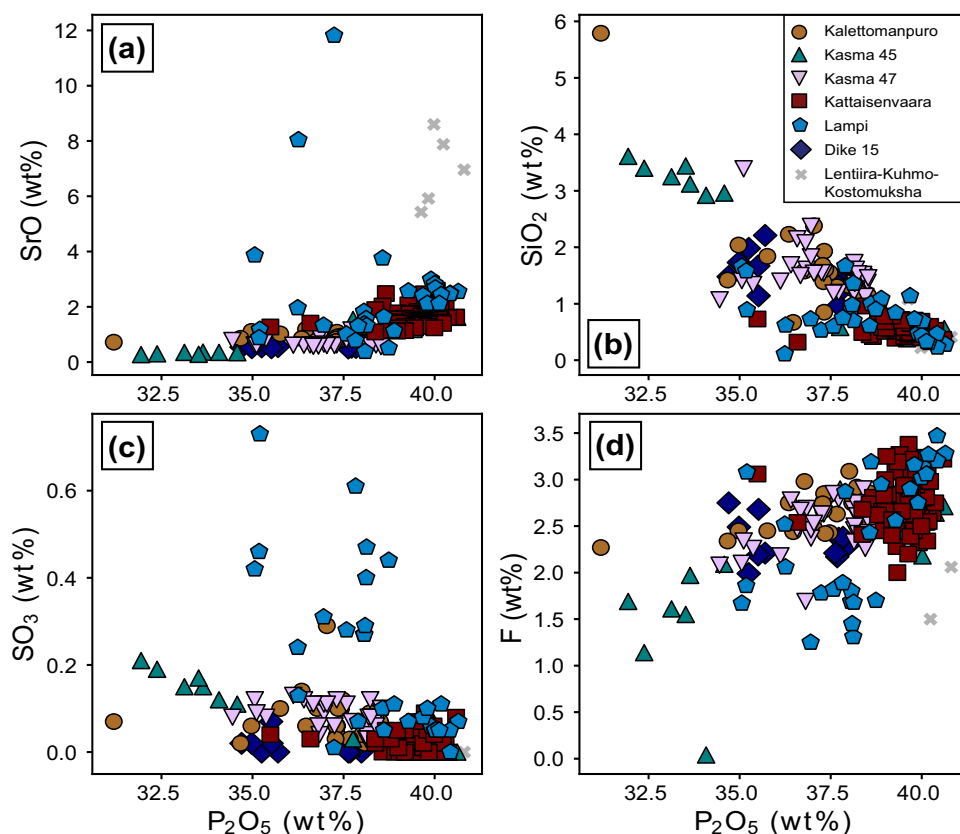
Fig. 9. (a) SrO vs P_2O_5, (b) SiO_2 vs P_2O_5, (c) SO_3 vs P_2O_5 and (d) F vs P_2O_5 co-variation plots for apatite in the Kuusamo rocks compared with apatite compositions from the Lentiira–Kuhmo–Kostomuksha orangeite cluster [data from Kargin *et al.* (2014)].

Lampi exhibit hydroxylapatite compositions (>0·5 a.p.f.u. OH).

Apatite in the Kasma and KP intrusions exhibits moderate to low SrO contents (<1·2 wt%), whereas apatite from KV is more enriched in SrO (1·1–2·6 wt%, Fig. 9a). The apatite from KV and Kasma 45/01 is therefore unlike 'typical' kimberlitic apatite, which is Sr-poor (SrO <1 wt%; Mitchell 1986), compared with apatite from orangeites and lamproites, which is comparatively enriched in Sr (e.g. Edgar, 1989; Mitchell & Bergman, 1991; Mitchell, 1995; Woolley *et al.*, 1996). Apatite compositions from the Kostomuksha and Kuhmo orangeites and lamproites are consistent with these observations (Fig. 9a). However, there are other examples of global kimberlites (e.g. Russia, West Africa, Canada) that contain high SrO (e.g. Tompkins, 1999; Beard *et al.*, 2000; Chakhmouradian *et al.*, 2002; Kopylova *et al.*, 2010).

As is the case for mica chemistry, apatite from Kasma 45 has prominent inter-sample variations; grains from KAS45/07, which contains Ba-rich mica (Supplementary Data Fig. S13), have an average SrO content of 0·32 ± 0·04 wt% and significant SiO_2 concentrations (up to 3·61 wt%). This contrasts with apatite from KAS45/01, which contains Ba-poor mica, and has an average SrO content of 1·5 ± 0·2 wt% and low SiO_2 concentrations (≤0·74 wt%). The elevated SiO_2 contents in KAS45/07 apatite coupled with low P_2O_5 (<35 wt%,

Fig. 9b), in all analyses across multiple thin sections, may be indicative of a coupled substitution involving CO_3, which could not be determined from current EPMA data (e.g. Sommerauer & Katz-Lehnert, 1985). A similar trend is observed for KV apatite, where grains from the shallower drill-core sample (26·85 m), which contains Ba-poor mica (Supplementary Data Fig. S13), hosts apatite with SrO contents that are on average ∼0·5 wt% higher than the deeper sample (33·85 m).

Lampi apatite exhibits a range in composition and is highly enriched in SrO (up to 11·8 wt% SrO; Fig. 9a) in the intermediate zones (see Fig. 3d). The apatite from Lampi is distinctive both in terms of variability and in elevated concentrations of SO_3 (up to 0·73 wt%) and Na_2O (up to 1·4 wt%; Supplementary Data Fig. S17) compared with the rocks described previously (≤0·29 wt% SO3; ≤0·33 wt% Na_2O).

Dike 15 apatite has lower SrO (0·54 ± 0·02 wt%), Na_2O (0·23 ± 0·07 wt%), and SO_3 (0·01 ± 0·02 wt%) contents, as well as moderate SiO_2 (1·5 ± 0·4 wt%) contents (Fig. 9) compared with the other intrusions.

Clinopyroxene

Clinopyroxene in the groundmass of Dike 15 has the composition of Fe-rich diopside (4·5–7·6 wt% FeO; 23·8–25·4 wt% CaO). Al_2O_3 and TiO_2 contents range from 0·6 to 2·5 wt% and from 0·8 to 3·0 wt%, respectively. Similar
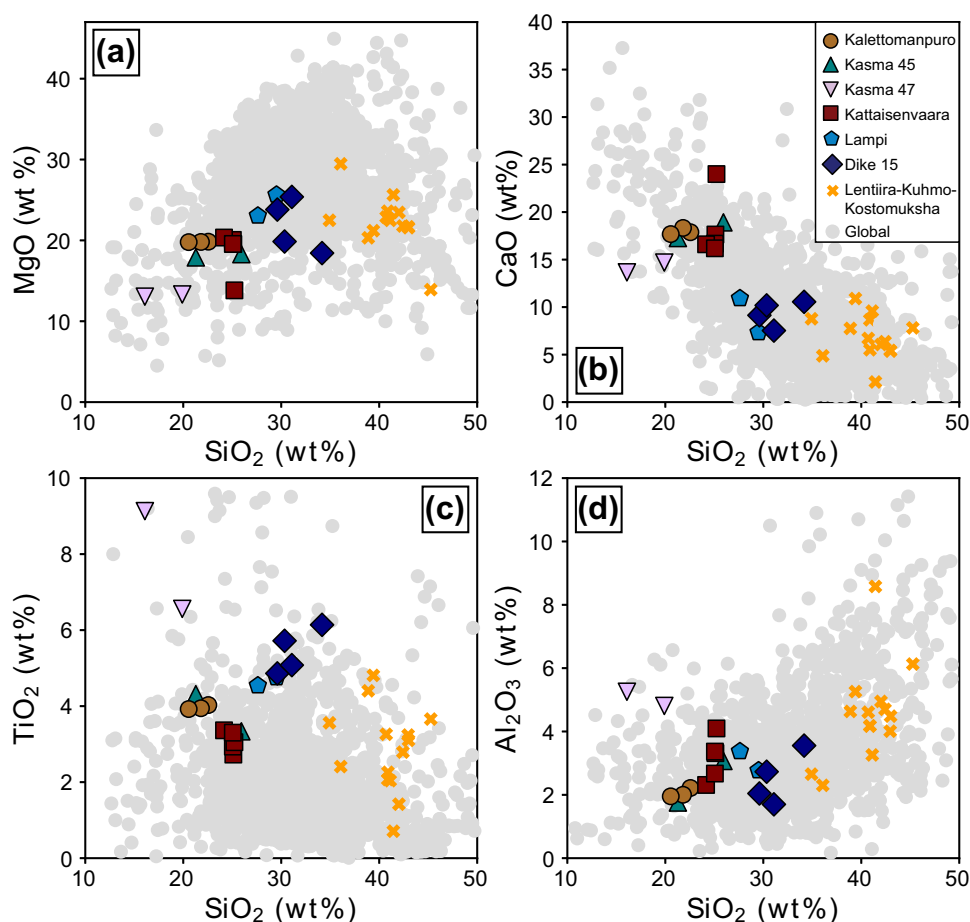
Fig. 10. (a) MgO vs SiO_2, (b) CaO vs SiO_2, (c) TiO_2 vs SiO_2 and (d) Al_2O_3 vs SiO_2 major element oxide co-variation plots for the Kuusamo rocks compared with compositions from the Lentiira–Kuhmo–Kostomuksha orangeites and lamproites (O'Brien & Tyni, 1999; Kargin *et al.*, 2014) and a global database of archetypal kimberlite bulk-rock compositions, which builds on that compiled by Kjarsgaard *et al.* (2009) and Tappe *et al.* (2017*b*) (see Supplementary Table S7 for data sources).

compositions are observed in clinopyroxene from UMLs emplaced at Aillik Bay, Canada (Tappe *et al.*, 2006).

WHOLE-ROCK GEOCHEMISTRY

The whole-rock major and trace element compositions of the Kuusamo intrusions are reported in Supplementary Data Table S7.

Major element geochemistry

Samples from KV, KP, and Kasma 45 have broadly similar bulk-rock major element compositions that are poor in MgO (13·8–20·4 wt%) and SiO_2 (20·6–26·0 wt%), and rich in CaO (16·2–24·0 wt%), whereas CO_2 contents are moderate to high (3·6–9·3 wt%). These also plot toward the lower limits for SiO_2 and MgO for kimberlites globally, whereas they are near the upper boundary for CaO contents (Fig. 10; Supplementary Data Fig. S18c). Kasma 47 is distinct from these samples and also notable for within-pipe variations; the oxide-rich zone (sample 28·6 m, Fig. 2h and i) is enriched in TiO_2

(9·1 vs 6·7 wt%) and Fe_2O_3 (26·7 vs 21·1 wt%) and contains less MgO (12·9 vs 13·5 wt%), SiO_2 (16·0 vs 20·2 wt%) and CO_2 (7·6 vs 8·5 wt%) compared with the olivine-rich sample (28·8 m; Fig. 5g and h; Supplementary Data Fig. S18). Lampi is enriched in SiO_2 and MgO relative to the above samples (27·6–29·5 wt% SiO_2, 23·1–25·6 wt% MgO), while being poorer in CaO (7·3–10·92 wt%). Dike 15 is distinguished by its high K_2O (up to 2·1 wt%) and MnO (up to 0·48 wt%), and low P_2O_5 (<0·8 wt%) contents relative to other Kuusamo intrusions. The CO_2 contents are not markedly different from those described above (3·9–7·3 wt%); however, the CO_2/K_2O ratios for these rocks are lower on average (3·9 vs 17; Supplementary Data Fig. S18). In addition, Dike 15 has the highest SiO_2 contents (29·6–34·2 wt%).

Trace element geochemistry

Transition metal contents for Lampi, KV, KP and the Kasma 45 bodies overlap closely, and define a limited range at the lower end of the global kimberlite compositional spectrum, with Ni and Cr contents of 221–
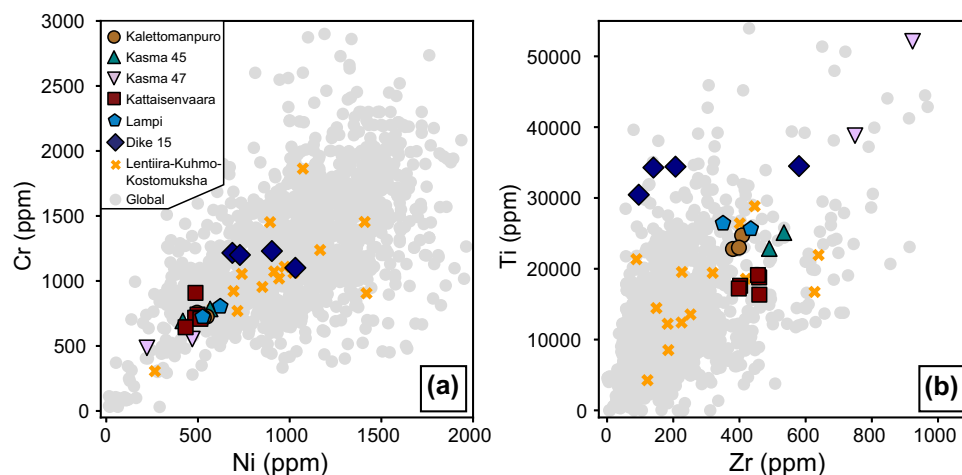
Fig. 11. (a) Cr vs Ni and (b) Ti vs Zr trace element co-variation plots for the Kuusamo rocks compared with compositions from the Lentiira–Kuhmo–Kostomuksha orangeites and lamproites (O'Brien & Tyni, 1999; Kargin *et al.*, 2014) and a global database of archetypal kimberlite bulk-rock compositions (see Supplementary Data Table S7 for sources).

621 ppm and 486–908 ppm, respectively (Fig. 11). In contrast, Dike 15 has considerably higher Ni (687–1031 ppm) and Cr (1101–1216 ppm) contents. The highly fluid-mobile elements such as Ba (325–5036 ppm) and Sr (88–2159 ppm) are variable when plotted against more immobile elements such as Nb (Supplementary Data Fig. S19). Similar to the major element variation in Kasma 47, the olivine-poor, oxide-rich sample is distinct in having lower concentrations of Ni (222 vs 469 ppm) but higher concentrations of Nb (628 vs 406 ppm) and Zr (923 vs 749 ppm) compared with the olivine-rich sample.

The Kuusamo rocks, excluding Dike 15, have significantly elevated levels of Sr, Hf, and Zr relative to kimberlites elsewhere. In particular, Kasma 47 is enriched in the high field strength elements (HFSE; e.g. Ti, Zr, Hf, Nb) compared with other Kuusamo intrusions and kimberlites generally. Primitive mantle-normalized trace element contents are also elevated relative to global kimberlites (Fig. 12), most notably in the heavy REE (HREE). The overall pattern indicates enrichment in the more incompatible elements (e.g. 40–880 times primitive mantle for Ba, Nb, and Ta) and pronounced negative anomalies at K and Sr, and more variably at Rb, Pb, Hf and Ti. These anomalies, which are typical of kimberlites, are generally lower in magnitude than for those observed elsewhere. This is particularly noticeable in the Kasma 47 samples, in which Zr–Hf anomalies are almost absent. Also notable is the variable magnitude of the Zr–Hf negative anomaly in the Dike 15 samples. The chondrite-normalized REE patterns plot towards enriched compositions compared with the global kimberlite dataset (Supplementary Data Fig. S20). Lampi (La$_N$/Yb$_N$ = 36–68) is displaced from the other Kuusamo bodies in terms of the light REE (LREE), with notably lower chondrite-normalized abundances for La to Sm. Overall though, there is a limited range in trace and rare earth element compositions.

GEOCHRONOLOGY OF DIKE 15

Rb–Sr analytical results for phlogopite in Dike 15 are reported in Supplementary Table S8. Bulk, residue and leachate fractions yield an isochron array (MSWD = 0·059) with an age of 1178 ± 4·1 Ma (95 % confidence limit) and ^{87}Sr/^{86}Sr$_i$ of 0·7035 ± 0·0001 (Supplementary Data Fig. S21). This age is broadly similar to ages reported for the Lentiira–Kuhmo–Kostomuksha orangeites and olivine lamproites (~1232–1180 Ma; Belyatskii *et al.*, 1997; O'Brien *et al.*, 2007; Phillips *et al.*, 2017*b*), and the isochron ^{87}Sr/^{86}Sr$_{(i)}$ for Dike 15 is indistinguishable from ^{87}Sr/^{86}Sr$_{(i)}$ values for whole-rock samples from Dike 15 (~0·7034 at 1178 Ma, recalculated using data from O'Brien & Tyni, 1999).

DISCUSSION

A 'hybrid' cluster of kimberlites and ultramafic lamprophyres

Classification of Kattaisenvaara, Kalettomanpuro, Kasma 45 and Kasma 47

Hypabyssal samples from KV, KP, Kasma 45 and Kasma 47 consist of altered olivine macrocrysts and microcrysts, and phlogopite phenocrysts in a groundmass of perovskite, apatite, spinel, ilmenite, serpentine and calcite. These petrographic features are typical of archetypal kimberlites (e.g. Mitchell, 1986, 2008). The mineral chemistry (Figs 5–9) is also consistent with this classification: phlogopite compositions are Al-rich and Ti–Fe-poor and typically show progressive rimward enrichment in Ba at decreasing Si and increasing Al (Fig. 5); spinel compositions evolve towards MUM spinel ending at magnetite (i.e. magmatic trend 1 or kimberlitic; Mitchell, 1986; Roeder & Schulze, 2008; Fig. 6); and perovskite is poor in REE. Although apatite from these rocks has SrO contents exceeding 1 wt%, which is unlike some kimberlites (Mitchell, 1986), apatite from other worldwide kimberlites (e.g. Russia, West Africa,
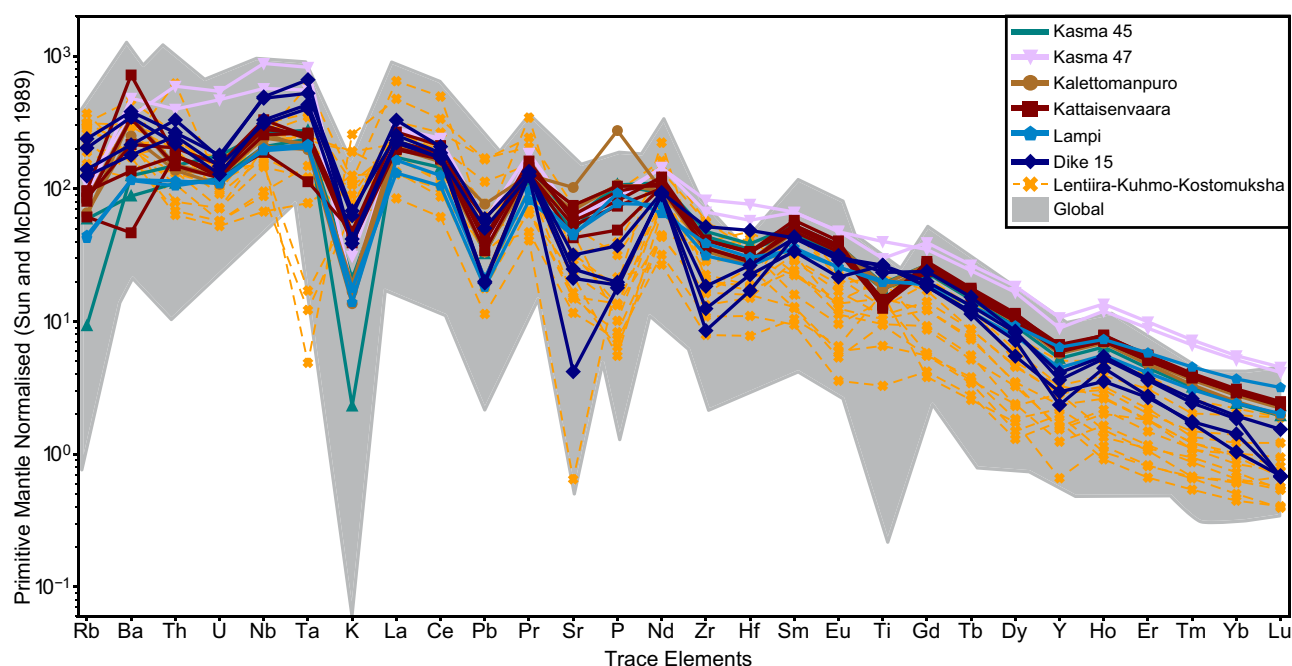
Fig. 12. Primitive mantle-normalized trace element plot for Kuusamo rocks compared with compositions from the Lentiira–Kuhmo–Kostomuksha orangeites and lamproites (O'Brien & Tyni, 1999; Kargin *et al.*, 2014) and a global database of archetypal kimberlite trace element compositions (see Supplementary Data Table S7 for sources). Normalising values from Sun and McDonough (1989).

Canada) exhibits SrO contents comparable with the Kuusamo samples (e.g. Tompkins, 1999; Beard *et al.*, 2000; Chakhmouradian *et al.*, 2002; Kopylova *et al.*, 2010).

With the exception of two KV samples, which are discussed further below, all the samples from KV, KP, and Kasma 45 have incompatible trace element ratios (La/Nb = 0·8 ± 0·1; Th/Nb = 0·07 ± 0·01; Ce/Pb = 45 ± 15; Nb/U = 66 ± 9) that strongly overlap with fields for archetypal kimberlites (Fig. 13). The elevated concentrations of HFSE in Kasma 47, which place these samples at the periphery of the kimberlite field in Fig. 13, reflects the greater abundance of oxide phases in these rocks (Fig. 2g–i) as well as indicating the potential influence of crustal contamination. This latter inference is also supported by the replacement of perovskite by anatase and titanite in Kasma 47, which requires elevated silica activity (e.g. Chakhmouradian & Mitchell, 2000; Martins *et al.*, 2014). Regardless, the combination of the above characteristics indicates that the KV, KP, Kasma 45, and Kasma 47 bodies can be interpreted as archetypal kimberlites.

Although classified as kimberlites, the Kuusamo intrusions exhibit unusual petrographic and geochemical features including: a paucity of olivine macrocrysts at <15 vol% compared with ∼25 vol% in archetypal kimberlites (e.g. Scott Smith *et al.*, 2013); the scarcity of mantle-derived xenocrysts including diamonds (Sunrise Diamonds PLC, 2010); the almost complete absence of chromite (i.e. TIMAC), which is the first spinel to crystallize from a kimberlitic melt (e.g. Mitchell, 2008; Soltys *et al.*, 2018); the predominance of evolved, Fe-rich, spinel compositions (e.g. MUM and Ti-magnetite);

and whole-rock compositions enriched in CaO (17·5 ± 2·4 wt%) and depleted in MgO (18·0 ± 2·7 wt%) compared with kimberlites worldwide (9·7 ± 5·4 wt% CaO, 27·0 ± 6·0 wt% MgO; Fig. 10). These features all attest to the evolved nature of the Kuusamo kimberlites, including pre-emplacement removal of magmatic chromite, macrocrystic olivine and other mantle-derived crystal cargo.

The Clement contamination index (C.I; Clement, 1982) was not employed here to deduce crustal contamination as the applicability of this index to such evolved rocks, or kimberlites outside of Southern Africa, is uncertain and the effects of magma differentiation are not explored. Further, recent work by Kjarsgaard *et al.* (2009) and Tappe *et al.* (2014) has raised concerns regarding the use of the index.

Lampi: a contaminated kimberlite

Although samples from the Lampi locality are petrographically distinct from the kimberlites described above, the spinel chemical trend (magmatic trend 1; Fig. 6) and the relatively large size and abundance of altered perovskite grains (>50 μm) are consistent with a kimberlitic, rather than an orangeitic or lamproitic paragenesis, where perovskite grains are both rarer and finer-grained (e.g. Skinner, 1989; Mitchell, 1995). In contrast, the Sr-rich composition of some Lampi apatite grains (and especially zones therein; Figs 2b and 9) is a feature more commonly observed in orangeites than kimberlites. In addition, the occurrence of euhedral, possibly magmatic, titanite (i.e. not pseudomorphs after perovskite; Fig. 3b) and resorbed quartz
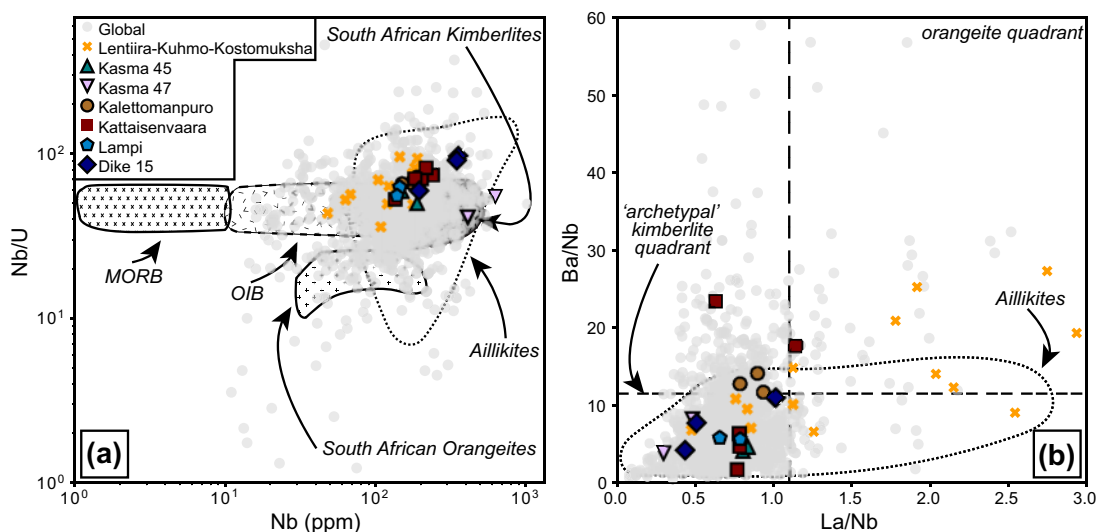
Fig. 13. (a) Nb/U vs Nb and (b) Ba/Nb vs La/Nb trace element ratio discriminatory co-variation plots for the Kuusamo rocks compared with compositions from the Lentiira–Kuhmo–Kostomuksha orangeites and lamproites (O'Brien & Tyni, 1999; Kargin *et al.*, 2014) and a global database of archetypal kimberlite trace element compositions (see Supplementary Data Table S7 for sources). Aillikite field is based on data from Tappe *et al.* (2004, 2006, 2008, 2011), Nielsen *et al.* (2009) and Donnelly *et al.* (2011). Discrimination fields for mid-ocean ridge basalt (MORB), ocean island basalt (OIB), kimberlites and orangeites after Becker & Le Roex (2006).

(Supplementary Data Fig. S8) is atypical of archetypal kimberlites. The chemical evolution of mica grains is another peculiarity in the Lampi rocks, defined by a core-to-rim trend of decreasing Ba, Al, and Ti with increasing Fe and Si (Fig. 5; see also Fig. 3c). This trend is essentially the inverse of what is considered 'typical' of kimberlitic mica, where Ba enrichment is confined to the rims rather than the cores of grains, and more closely resembles the evolutionary trend of orangeites (e.g. Mitchell, 1995; Giuliani *et al.*, 2016). Although rare in kimberlites, analogous zonation patterns have been noted in mica from discrete segregations in the Aries kimberlite (e.g. Downes *et al.*, 2006) and in poikilitic phlogopite from the Snap Lake (Mogg *et al.*, 2003; Kopylova *et al.*, 2010), Gahcho Kue (Caro *et al.*, 2004) and Lac de Gras kimberlites (Chakhmouradian *et al.*, 2002) in Canada, as well as kimberlites from the Arkhangelsk region (Beard *et al.*, 2000). The Ba enrichment in Lampi phlogopite cores precludes crystallization at high pressure, because Ba can only be incorporated into phlogopite at low pressure and high temperature (e.g. Guo & Green, 1990; Righter & Carmichael, 1996; Gaeta *et al.*, 2000). Rather, the enrichment in Ba of mica in kimberlites and related rocks requires crystallization from a highly differentiated melt (e.g. see rimward enrichment in Ba in mica from other Kuusamo samples). The evolved nature of the melt parental to Lampi is consistent with the rarity of olivine macrocrysts and other mantle xenocrysts in this occurrence (including diamonds; Sunrise Diamonds PLC, 2014), and is similar to the Kuusamo kimberlites described above. However, this alone cannot explain the unusual mica evolutionary trend and the other petrographic oddities of Lampi.

In the Gahcho Kue kimberlite, mica evolution from Ba-rich cores towards compositions typical of orangeite micas is attributed to contamination by granitic xenoliths (Caro *et al.*, 2004). It is plausible that assimilation of country rock also contributed to the rimward Si and Fe enrichment in the Lampi mica grains (e.g. Chakhmouradian & Mitchell, 2000). Interaction of the Lampi magma with crustal material is also supported by elevated whole-rock SiO_2 contents (up to 29·5 wt%), low Nb (up to 144 ppm; Supplementary Data Fig. S19), and low La_N/Yb_N (36–68; Supplementary Data Fig. S20), compared with other Kuusamo kimberlites. Crustal rocks are typically poor in Nb and have relatively flat HREE patterns with greater HREE abundances compared with kimberlite. Therefore crustal contamination of kimberlite magmas is expected to dilute Nb contents and flatten REE patterns (e.g. Rudnick & Fountain, 1995; Le Roex *et al.*, 2003) as for the Lampi samples. The occurrence of xenocrystic quartz and primary titanite is also consistent with crustal contamination. The coexistence of titanite and monticellite (Fig. 3) in the groundmass of Lampi is unusual as these minerals are stable at different silica activities ($aSiO_2$); that is, titanite crystallizes at elevated $aSiO_2$ relative to monticellite (e.g. Barker, 2001). Therefore, it is suggested that crustal contamination (and hence elevated SiO_2 levels) occurred late in the crystallization sequence of Lampi (i.e. after monticellite crystallization).

Assimilation of granitoid material should also increase oxygen fugacity (fO_2) levels, which is consistent with the increasing tetraferriphlogopite component in mica overgrowths, and the elevated SO_3 contents of Lampi apatite (i.e. an order of a magnitude greater than for the other Kuusamo rocks; Fig. 9). Increasing fO_2 is thought to promote the incorporation of S into the

apatite structure in the S^{6+} oxidation state (e.g. Peng et al., 1997; Wang et al., 2014). The replacement of P^{5+} by S^{6+} can follow two coupled substitution mechanisms involving Na and Si (Rouse & Dunn, 1982; Liu & Comodi, 1993; Pan & Fleet, 2002). This substitution is indicated in the Lampi apatite, where all grains with elevated SO_3 (≥ 0.13 wt%) also have elevated Na_2O (>0.29 wt%; Supplementary Data Fig. S17b).

Although the petrographic and mineral chemical features of the Lampi locality are somewhat intermediate between those of kimberlites and orangeites, and may indicate a paradoxical petrogenesis for Lampi rocks, the bulk-rock trace element ratios (La/Nb = 0.7 ± 0.1; Th/Nb = 0.07 ± 0.01; Ce/Pb = 56 ± 1) overlap with those of global kimberlites and are distinct from orangeites, including samples from Lentiira, Kuhmo, and Kostomuksha (Fig. 13). Similarly, the Lampi trace element patterns are typical of kimberlitic rocks (Fig. 12). The Lampi intrusion is therefore classified as an evolved kimberlite, but one that has undergone significant crustal assimilation, such that some of the 'typical' kimberlite hallmarks are modified. It is evident from this example that successful identification and classification of similar ultramafic alkaline rocks requires a complete petrographic examination in conjunction with chemical analyses to disentangle the influence of pre-, syn- or post-emplacement processes.

Dike 15 aillikite

Samples from Dike 15 are composed of zoned phenocrysts of phlogopite as well as less abundant macrocrysts and phenocrysts of altered olivine set in a groundmass of apatite, clinopyroxene, ilmenite, spinel and prominent carbonate. With the exception of clinopyroxene, the majority of these constituents are also common to kimberlites; however, the proportions of these minerals (e.g. phlogopite enrichment) as well as their chemistry indicate that Dike 15 is not a kimberlite. For example, phlogopite compositions overlap with those of UMLs (Fig. 5), and spinel compositions follow magmatic trend 2 (Fig. 9; i.e. non-kimberlitic, Mitchell, 1986; Roeder & Schulze, 2008), a feature that typifies UMLs globally (e.g. Rock, 1991; Tappe et al., 2004, 2006; Nielsen et al., 2009). Finally, the presence of Sr-poor apatite (<0.6 wt%), Mn-rich ilmenite (up to 9.0 wt%) and Fe–Ti–Al-rich diopside are all typical of UMLs (e.g. Rock, 1987, 1991; Seifert et al., 2000; Tappe et al., 2004, 2005).

Although the bulk compositions of Dike 15 samples lie within the kimberlite fields in Fig. 13, these compositions also overlap with those typical of UMLs (e.g. Ba/Nb = 2–14 and La/Nb up to 2.7 for Greenland–Labrador UMLs; Tappe et al., 2008). Dike 15 exhibits notably lower concentrations of HREE (Supplementary Data Fig. S20) compared with the Kuusamo kimberlites and consequently has a steeper chondrite-normalized REE pattern (La_N/Yb_N = 125–232 vs 36–91). Although UMLs typically exhibit shallower REE profiles compared with kimberlites (e.g. Rock, 1986, 1991; Donnelly et al., 2011),

the strong REE fractionation observed for Dike 15 has been observed for UMLs in the North Atlantic Alkaline Province (La_N/Yb_N = 58–204; Tappe et al., 2004). The combination of petrographic and compositional data from our study indicates that Dike 15 should therefore be classified as a carbonate-rich UML, of type aillikite (e.g. Tappe et al., 2005).

Multiple magma batches in the Kuusamo bodies

Kattaisenvaara and Kasma 45

The majority of the Kuusamo kimberlites host mica grains that closely follow the 'typical' kimberlitic evolutionary trend. However, phlogopite from Kattaisenvaara (KV) is unique because of the coexistence of grains displaying rimward enrichment of Ba and grains exhibiting reverse zoning from Ba–Al-rich cores to Ba–Al-poor rims. In addition, there are KV samples where the BaO content of phlogopite is very low (Fig. 3; Supplementary Data Fig. S13). Such contrasting phlogopite chemistries within the same body may result from mixing of different batches of variably evolved kimberlite magmas (e.g. Mogg et al., 2003; Kopylova et al., 2010). It is envisaged that a more evolved early batch generated the Ba–Al-rich cores, which were subsequently overgrown by Ba–Al-poor rims from a later, more 'primitive' melt. The development of concentric zoning in phlogopite is also unique to this kimberlite, and may be due to changes in local temperature and bulk composition of the melt (e.g. Allègre et al., 1981; Shore & Fowler, 1996). Significantly, oscillatory zoning in perovskite is similarly unique to KV. Such zonation is also thought to be typical of crystal growth in an open system following magma mixing (Holten et al., 2000), which is consistent with the intra-kimberlite variations observed for phlogopite (Supplementary Data Fig. S13), apatite (Fig. 9) and spinel (Supplementary Data Fig. S14) from KV. Finally, the contrasting whole-rock Ba contents (Supplementary Data Fig. S17) of KV might also support crystallization from different magma batches.

Similar to KV, prominent mica variations exist between two samples in the Kasma 45 kimberlite (e.g. average BaO contents differ by 6.3 wt%; Supplementary Data Fig. S13), and this pipe may also have developed from multiple magma batches. For both KV and Kasma 45 the composition of apatite varies in conjunction with mica composition, and lends support to this hypothesis; that is, SrO-richer apatite is associated with samples hosting Ba-poorer mica (see Mineral Chemistry section).

Kasma 47 hypabyssal kimberlite

The petrographic and geochemical variations observed at Kasma 47 provide insight into its formation. This hypabyssal kimberlite (~0.8 m thick) is overlain by tens of metres of volcaniclastic material, whereas country rock is observed at the lower contact. It was noted above that the petrographic, 'cumulate-like' variations

within this hypabyssal unit (Fig. 2g–i) are similar to those observed in the Benfontein and Wesselton kimberlite sills in South Africa, and the Kasma 47 parental magma may have shared a similar emplacement process (Dawson & Hawthorne, 1973; Abersteiner et al., 2019). The olivine-rich sample of Kasma 47 (28·8 m; Fig. 2g and h) has elevated whole-rock Ni concentrations (469 vs 222 ppm), as well as lower concentrations of MgO in both spinel (9·6 ± 0·7 vs 11·0 ± 0·6 wt%; Supplementary Data Fig. S14) and ilmenite (11·5 ± 0·9 vs 13·0 ± 0·6 wt%) when compared with the olivine-poor sample (28·6 m; Fig. 2h-i), consistent with the uptake of Ni and MgO by olivine. In addition, the olivine-poor sample has elevated HFSE (Fig. 10; Supplementary Data Fig. S19) consistent with accumulation of oxide phases. It is possible that these petrographic and geochemical variations represent the product of multiple batches of magma or pre- and/or syn-emplacement magma differentiation by crystal fractionation (e.g. Dawson & Hawthorne, 1973; White et al., 2012; Abersteiner et al., 2019). The sharp contact between olivine-rich and olivine-poor zones in one of the examined samples (Fig. 2h) favours the former option, which is similar to the mechanism proposed for KV and Kasma 45.

Macrocrystic phlogopite in Dike 15

Dike 15 aillikite samples contain macrocrysts of phlogopite with inclusion-free cores (Fig. 4b; Supplementary Data Fig. S11) of high Ti–Cr composition, which are distinct from the phenocrysts and macrocryst rims from this intrusion (Fig. 5). These cores may be xenocrysts, derived from the mantle or crustal country rock, or they may be linked to similar, but earlier, magmatic events. The composition of these cores (7·5 ± 0·4 wt% TiO_2; 1·0 ± 0·2 wt% Cr_2O_3) does not overlap with phlogopite in mantle xenoliths (Fitzpayne et al., 2018, and references therein) nor is it consistent with mica compositions in host granitoids (i.e. biotite). High Ti–Cr zones in phlogopites observed in kimberlitic rocks elsewhere have been ascribed to antecrysts from previous, 'failed' batches of kimberlite magma that have been sampled by a subsequent 'successful' kimberlite on ascent to surface (e.g. Giuliani et al., 2016). In the absence of an alternative explanation, we suggest that the resorbed, high Ti–Cr cores of phlogopite macrocrysts in Dike 15 are antecrysts related to previous injections of aillikite magma into the upper mantle or lower crust (see also Tappe et al., 2006). These xenocrysts were then subsequently entrained by Dike 15 magma, partially resorbed and formed the nuclei for precipitation of later generations of poikilitic phlogopite. It is now widely recognized (e.g. Giuliani et al., 2014, 2016; Aulbach et al., 2018) that mantle preconditioning by previously 'failed' kimberlites has an important role in facilitating the eruptive success of later kimberlite magmas and we posit that similar processes may result in the emplacement of ultramafic lamprophyres into the crust.

Genesis of a 'hybrid' cluster

The Kuusamo cluster exhibits a close spatial association of variable lithologies, including an ultramafic lamprophyre (Dike 15), and variably evolved kimberlites. The juxtaposition of alkaline ultramafic rocks (including UML, orangeites, carbonatites and kamafugites) and kimberlites is not unique to Finland, as similar associations occur in southern Africa, Western and Southern Australia, West Greenland–Labrador, Brazil, Russia and India (e.g. Scott-Smith et al., 1984; Fielding & Jaques, 1986; Gibson et al., 1995; Beard et al., 1996; Graham et al., 2004; Downes et al., 2005; Tappe et al., 2008; Hutchison & Frei, 2009; Donnelly et al., 2011; Guarino et al., 2013; Smith et al., 2013). Where spatio-temporal overlap is well constrained, genetic links or potential transitions or continua between mantle-derived magmas are often inferred. Based on the geochronological evidence presented here, it is evident that the kimberlites post-date the UML (Dike 15) emplacement by >450 Myr. Below we discuss possible mechanisms for the coexistence of ultramafic lamprophyre and kimberlite magmas in the Kuusamo cluster and also address the contemporaneous emplacement of Dike 15 with the nearby (∼100 km SE) Lentiira–Kuhmo–Kostomuksha orangeites and olivine-lamproites (Fig. 1).

Spatial association of kimberlites and ultramafic lamprophyres with no genetic link

The strong overlap in incompatible element ratios between the Kuusamo kimberlites, Dike 15, and those worldwide (as well as ocean island basalts; Fig. 13) suggests that they share a similar mantle source, which is likely to be the asthenospheric mantle (e.g. Smith, 1983; Nowell et al., 2004; Tappe et al., 2011, 2013; Sun et al., 2014; Woodhead et al., 2017). However, given the ∼450 Myr time delay observed on the Karelian craton it is difficult to postulate a direct genetic link between the genesis of Dike 15 and that of the kimberlites.

Their spatial overlap is probably a consequence of the ascending magmas exploiting the same or similar trans-lithospheric structures. NE–SW-oriented faults linked to a large-scale (>100 km in length; Fig. 1) shear zone are known for the Precambrian basement in the Kuusamo region (Laajoki, 2005). These structures may have facilitated the successful emplacement of both the kimberlites and the Dike 15 UML in the Kuusamo cluster, which is also oriented in a corridor striking generally NNE–SSW (Fig. 1). Similarly, the emplacement of kimberlites and alkaline ultramafic magmas globally has long been thought to be controlled by the position of large-scale structures (e.g. Williams & Williams, 1977; Parrish & Lavin, 1982; White et al., 1995; Phillips et al., 1998; Jelsma et al., 2004, 2009). As a possible result of this phenomenon, there are examples in West Greenland–Labrador (e.g. Tappe et al., 2007), southern Africa (e.g. Clement et al., 1979; Donnelly et al., 2011) and India (e.g. Chalapathi Rao et al., 2016) where
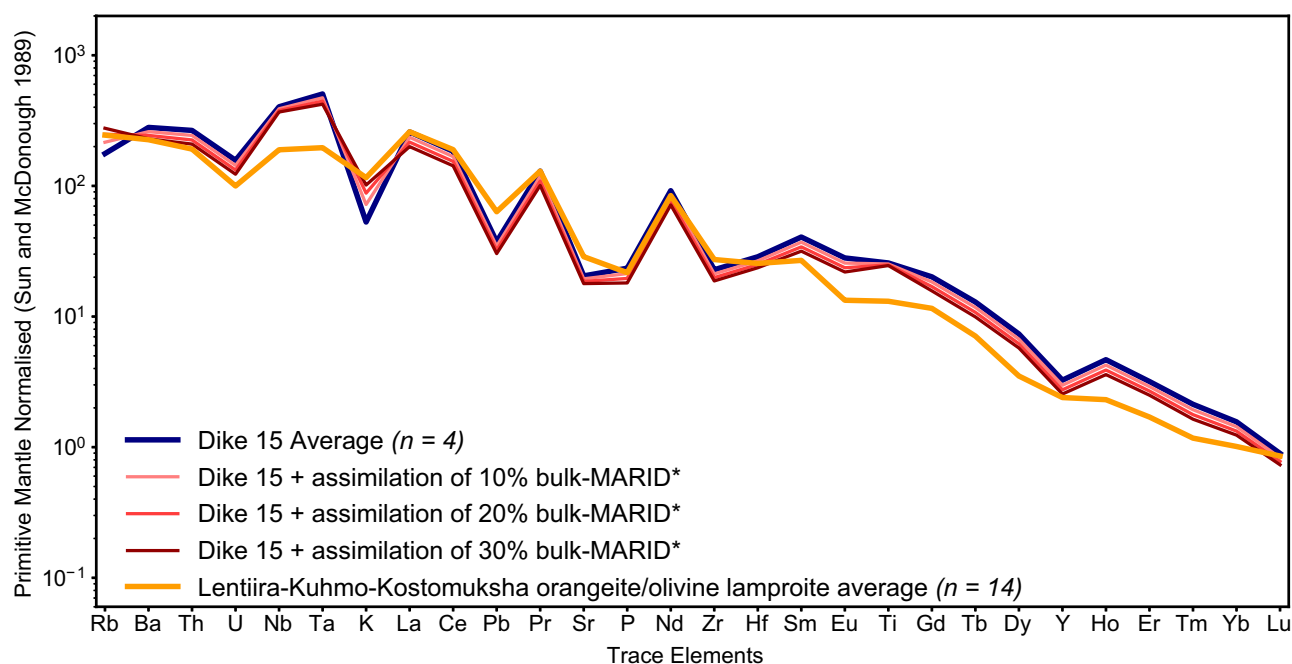
Fig. 14. Primitive mantle-normalized trace element plots comparing the average composition of Dike 15 and the Lentiira–Kuhmo–Kostmuksha orangeites and olivine lamproites [data from Kargin *et al.* (2014)]. The composition of Dike 15 approaches that of the orangeites and olivine lamproites upon increasing the degree of assimilation of metasomatized lithospheric mantle material as proxied by MARID-type rocks (*composition from Fitzpayne *et al.*, 2018).

ultramafic magmas of varying composition overlap closely in space but not in time.

Petrogenetic relationship between Dike 15 and olivine lamproite magmatism on the Karelian craton

It is evident from this study that Dike 15 exhibits temporal overlap with the emplacement of the proximal Lentiira–Kuhmo–Kostomuksha orangeites and olivine lamproites (Fig. 1); that is, 1178 ± 4 Ma (this study) vs 1204 ± 4 Ma to 1180 ± 5 Ma (O'Brien *et al.*, 2007; Phillips *et al.*, 2017*b*). Therefore, we suggest that Dike 15 represents an important additional example of Mesoproterozoic alkaline ultramafic magmatism on the Karelian craton. It has been previously proposed that the genesis of the Lentiira–Kuhmo–Kostomuksha rocks involved derivation from a metasomatized, phlogopite and K-richterite-bearing lithospheric mantle, with melting triggered by influx of an asthenospheric melt (e.g. Belyatskii *et al.*, 1997; O'Brien & Tyni, 1999; O'Brien *et al.*, 2005; Kargin *et al.*, 2014). We therefore envisage that Dike 15 represents a manifestation of similar asthenosphere-derived melts.

The viability of the above scenario can therefore be assessed by modelling the interaction of Dike 15 with metasomatized lithospheric mantle material. Importantly, geothermobarometric and geochemical studies carried out on xenocrysts and diamonds derived from Finnish kimberlites reveal that the Karelian craton lithosphere is both stratified and metasomatized, with an ~ 100 km thick metasomatized lower layer noted beneath Kuusamo (Lehtonen & O'Brien, 2009; Smart *et al.*,

2017). We utilize a 'bulk-MARID' composition (Fitzpayne *et al.*, 2018) as a proxy for the composition of this metasomatized lithospheric mantle and model how assimilation of such material alters the composition of Dike 15 magmas. We note that upon increasing proportions of enriched lithospheric mantle assimilation, Dike 15 compositions gradually approach the average composition of the Lentiira–Kuhmo–Kostomuksha orangeites and olivine lamproites (Fig. 14). The low CO_2/K_2O of these latter rocks relative to Dike 15 (Supplementary Data Fig. S18) is also compatible with an enhanced involvement of metasomatized lithosphere in their genesis (e.g. Tappe *et al.*, 2011). Based on this evidence and the strong temporal overlap, we conclude that there is an intimate link between UML and orangeite–lamproite emplacement on the Karelian craton.

CONCLUSIONS

This study includes the first comprehensive petrographic, mineral and whole-rock geochemical results for the Kuusamo cluster, the most recently discovered kimberlite cluster in Europe. The petrographic observations and geochemical data permit the classification of the Kattaisenvaara (KV), Kalettomanpuro (KP), Kasma 45, Kasma 47, and Lampi intrusions as evolved kimberlites, which is consistent with the low diamond potential of the Kuusamo kimberlites. Lampi exhibits unique features, including elevated bulk-rock SiO_2 contents, presence of titanite and quartz, and mica compositions that trend towards orangeite–lamproite compositions, which are attributed to crustal contamination, probably

during or after kimberlite emplacement in the upper crust. These kimberlites are spatially associated with Dike 15, which is a carbonate-rich rock with petrographic and geochemical features characteristic of ultramafic lamprophyres, specifically aillikites. Variations in mineral and whole-rock geochemistry as well as mineral abundances across multiple samples from numerous intrusions provide strong evidence of multiple pulses of magmatic activity at the hand-specimen and mineral scale. High Ti–Cr antecrystic cores in phlogopite macrocrysts from Dike 15 indicate that this intrusion resulted from repeated magmatic activity.

The first radiometric age presented here for Dike 15 indicates a temporal relationship with the Lentiira–Kuhmo–Kostmuksha orangeites and olivine lamproites. We suggest that this relationship may also be genetic, whereby Dike 15-like (aillikitic) magmas were modified by significant interaction with enriched lithospheric mantle material, resulting in compositions similar to those observed in the orangeites and olivine lamproites, which were emplaced for ∼20 Myr following Dike 15. The ∼450 Myr time gap between the Kuusamo kimberlites emplacement and Dike 15 suggests that a genetic relationship may not exist, but instead their proximity to one another is a function of exploiting similar lithospheric corridors on ascent to surface.

ACKNOWLEDGEMENTS

FUNDING

SUPPLEMENTARY DATA

REFERENCES

Abersteiner, A., Kamenetsky, V. S., Goemann, K., Giuliani, A., Howarth, G. H., Castillo-Oliver, M., Thompson, J., Kamenetsky, M. & Cherry, A. (2019). Composition and emplacement of the Benfontein kimberlite sill complex (Kimberley, South Africa): Textural, petrographic and melt inclusion constraints. *Lithos* **324–32d5**, 297–314.

Allègre, C. J., Provost, A. & Jaupart, C. (1981). Oscillatory zoning: a pathological case of crystal growth. *Nature* **294**, 223–228.

Armstrong, J. P., Wilson, M., Barnett, R. L., Nowicki, T. & Kjarsgaard, B. A. (2004). Mineralogy of primary carbonate-bearing hypabyssal kimberlite, Lac de Gras, Slave Province, Northwest Territories, Canada. *Lithos* **76**, 415–433.

Aulbach, S., Creaser, R. A., Stachel, T., Heaman, L. M., Chinn, I. L. & Kong, J. (2018). Diamond ages from Victor (Superior Craton): intra-mantle cycling of volatiles (C, N, S) during supercontinent reorganisation. *Earth and Planetary Science Letters* **490**, 77–87.

Barker, D. S. (2001). Calculated silica activities in carbonatite liquids. *Contributions to Mineralogy and Petrology* **141**, 704–709.

Beard, A. D., Downes, H., Vetrin, V., Kempton, P. D. & Maluski, H. (1996). Petrogenesis of Devonian lamprophyre and carbonatite minor intrusions, Kandalaksha Gulf (Kola Peninsula, Russia). *Lithos* **39**, 93–119.

Beard, A. D., Downes, H., Hegner, E., Sablukov, S. M., Vetrin, V. R. & Balogh, K. (1998). Mineralogy and geochemistry of Devonian ultramafic minor intrusions of the southern Kola Peninsula, Russia: implications for the petrogenesis of kimberlites and melilitites. *Contributions to Mineralogy and Petrology* **130**, 288–303.

Beard, A. D., Downes, H., Hegner, E. & Sablukov, S. M. (2000). Geochemistry and mineralogy of kimberlites from the Arkhangelsk Region, NW Russia: evidence for transitional kimberlite magma types. *Lithos* **51**, 47–73.

Becker, M. & Le Roex, A. P. (2006). Geochemistry of South African on- and off-craton, group I and group II kimberlites: petrogenesis and source region evolution. *Journal of Petrology* **47**, 673–703.

Bell, K. & Simonetti, A. (2010). Source of parental melts to carbonatites—critical isotopic constraints. *Mineralogy and Petrology* **98**, 77–89.

Belyatskii, B., Nikitina, L., Savva, E. & Levskii, L. (1997). Isotopic signatures of lamproite dikes on the eastern Baltic Shield. *Geochemistry International* **35**, 575–579.

Caro, G., Kopylova, M. G. & Creaser, R. A. (2004). The hypabyssal 5034 kimberlite of the Gahcho Kue cluster, southeastern Slave craton, Northwest Territories, Canada: a granite-contaminated Group-I kimberlite. *Canadian Mineralogist* **42**, 183–207.

Castillo-Oliver, M., Melgarejo, J. C., Galí, S., Pervov, V., Gonçalves, A. O., Griffin, W. L., Pearson, N. J. & O'Reilly, S. Y. (2017). Use and misuse of Mg- and Mn-rich ilmenite in diamond exploration: a petrographic and trace element approach. *Lithos* **292–293**, 348–363.

Castillo-Oliver, M., Giuliani, A., Griffin, W. L. & O'Reilly, S. Y. (2018). Characterisation of primary and secondary carbonates in hypabyssal kimberlites: an integrated

compositional and Sr-isotopic approach. *Mineralogy and Petrology* **112**, 555–567.

Chakhmouradian, A. R. & Mitchell, R. H. (2000). Occurrence, alteration patterns and compositional variation of perovskite in kimberlites. *Canadian Mineralogist* **38**, 975–994.

Chakhmouradian, A. R., Reguir, E. P. & Mitchell, R. H. (2002). Strontium-apatite: new occurrences, and the extent of Sr-for-Ca substitution in apatite-group minerals. *Canadian Mineralogist* **40**, 121–136.

Chalapathi Rao, N. V. & Lehmann, B. (2011). Kimberlites, flood basalts and mantle plumes: new insights from the Deccan Large Igneous Province. *Earth-Science Reviews* **107**, 315–324.

Chalapathi Rao, N. V., Dongre, A., Wu, F.-Y. & Lehmann, B. (2016). A late Cretaceous (*ca.* 90 Ma) kimberlite event in southern India: implication for sub-continental lithospheric mantle evolution and diamond exploration. *Gondwana Research* **35**, 378–389.

Clement, C. R. (1982). *A Comparative Geological Study of Some Major Kimberlite Pipes in the Northern Cape and Orange Free State*. Cape Town: University of Cape Town, 728 pp.

Clement, C. R., Skinner, E. M. W., Hawthorne, J. B., Kleinjan, L. & Allsopp, H. L. (1979). Precambrian ultramafic dykes with kimberlite affinities in the Kimberley area. In: Meyer, H. O. A. & Boyd, F. (eds) *Kimberlites, Diatremes, and Diamonds: Their Geology, Petrology, and Geochemistry; Proceedings of the 2nd Kimberlite Conference*. Washington, DC: American Geophysical Union, pp. 101–110.

Dalton, H., Giuliani, A., O'Brien, H., Phillips, D. & Hergt, J. (2020). The role of lithospheric heterogeneity on the composition of kimberlite magmas from a single field: The case of Kaavi-Kuopio, Finland. *Lithos* **354-355**, 105333.

Dawson, J. B. & Hawthorne, J. B. (1973). Magmatic sedimentation and carbonatitic differentiation in kimberlite sills at Benfontein, South Africa. *Journal of the Geological Society, London* **129**, 61–85.

Dongre, A. & Tappe, S. (2019). Kimberlite and carbonatite dykes within the Premier diatreme root (Cullinan Diamond Mine, South Africa): new insights to mineralogical–genetic classifications and magma CO_2 degassing. *Lithos* **338–339**, 155–173.

Donnelly, C. L., Griffin, W. L., O'Reilly, S. Y., Pearson, N. J. & Shee, S. R. (2011). The kimberlites and related rocks of the Kuruman Kimberlite Province, Kaapvaal Craton, South Africa. *Contributions to Mineralogy and Petrology* **161**, 351–371.

Downes, H., Balaganskaya, E., Beard, A., Liferovich, R. & Demaiffe, D. (2005). Petrogenetic processes in the ultramafic, alkaline and carbonatitic magmatism in the Kola Alkaline Province: A review. *Lithos* **85**, 48–75.

Downes, P. J., Wartho, J.-A. & Griffin, B. J. (2006). Magmatic evolution and ascent history of the Aries micaceous kimberlite, Central Kimberley Basin, Western Australia: evidence from zoned phlogopite phenocrysts, and UV laser $^{40}Ar/^{39}Ar$ analysis of phlogopite–biotite. *Journal of Petrology* **47**, 1751–1783.

Duke, G. I., Carlson, R. W., Frost, C. D., Hearn, B. C., Jr & Eby, G. N. (2014). Continent-scale linearity of kimberlite–carbonatite magmatism, mid-continent North America. *Earth and Planetary Science Letters* **403**, 1–14.

Edgar, A. D. (1989). Barium- and strontium-enriched apatites in lamproites from West Kimberley, Western Australia. *American Mineralogist* **74**, 889–895.

Eggins, S. M., Woodhead, J. D., Kinsley, L. P. J., Mortimer, G. E., Sylvester, P., McCulloch, M. T., Hergt, J. M. & Handler, M. R. (1997). A simple method for the precise determination of $\geq$ 40 trace elements in geological samples by ICPMS using enriched isotope internal standardisation. *Chemical Geology* **134**, 311–326.

Exley, R. A. & Jones, A. P. (1983). $^{87}Sr/^{86}Sr$ in kimberlitic carbonates by ion microprobe: Hydrothermal alteration, crustal contamination and relation to carbonatite. *Contributions to Mineralogy and Petrology* **83**, 288–292.

Field, M., Stiefenhofer, J., Robey, J. & Kurszlaukis, S. (2008). Kimberlite-hosted diamond deposits of southern Africa: A review. *Ore Geology Reviews* **34**, 33–75.

Fielding, D. & Jaques, A. (eds) (1986). *Geology, Petrology and Geochemistry of the Bow Hill Lamprophyre Dykes*. Perth, WA: Geological Society of Australia.

Fitzpayne, A., Giuliani, A., Hergt, J., Phillips, D. & Janney, P. (2018). New geochemical constraints on the origins of MARID and PIC rocks: Implications for mantle metasomatism and mantle-derived potassic magmatism. *Lithos* **318–319**, 478–493.

Foley, S. F., Andronikov, A. V. & Melzer, S. (2002). Petrology of ultramafic lamprophyres from the Beaver Lake area of Eastern Antarctica and their relation to the breakup of Gondwanaland. *Mineralogy and Petrology* **74**, 361–384.

Gaeta, M., Fabrizio, G. & Cavarretta, G. (2000). F-phlogopites in the Alban Hills Volcanic District (Central Italy): indications regarding the role of volatiles in magmatic crystallisation. *Journal of Volcanology and Geothermal Research* **99**, 179–193.

Gaspar, J. C. & Wyllie, P. J. (1984). The alleged kimberlite–carbonatite relationship: evidence from ilmenite and spinel from Premier and Wesselton mines and the Benfontein sill, South Africa. *Contributions to Mineralogy and Petrology* **85**, 133–140.

Gibson, S. A., Thompson, R. N., Leonardos, O. H., Dickin, A. P. & Mitchell, J. G. (1995). The Late Cretaceous impact of the Trindade mantle plume: evidence from large-volume, mafic, potassic magmatism in SE Brazil. *Journal of Petrology* **36**, 189–229.

Giuliani, A., Phillips, D., Kamenetsky, V. S., Kendrick, M. A., Wyatt, B. A., Goemann, K. & Hutchinson, G. (2014). Petrogenesis of mantle polymict breccias: insights into mantle processes coeval with kimberlite magmatism. *Journal of Petrology* **55**, 831–858.

Giuliani, A., Phillips, D., Woodhead, J. D., Kamenetsky, V. S., Fiorentini, M. L., Maas, R., Soltys, A. & Armstrong, R. A. (2015). Did diamond-bearing orangeites originate from MARID-veined peridotites in the lithospheric mantle? *Nature Communications* **6**, 6837.

Giuliani, A., Phillips, D., Kamenetsky, V. S. & Goemann, K. (2016). Constraints on kimberlite ascent mechanisms revealed by phlogopite compositions in kimberlites and mantle xenoliths. *Lithos* **240–243**, 189–201.

Giuliani, A., Soltys, A., Phillips, D., Kamenetsky, V. S., Maas, R., Goemann, K., Woodhead, J. D., Drysdale, R. N. & Griffin, W. L. (2017). The final stages of kimberlite petrogenesis: Petrography, mineral chemistry, melt inclusions and Sr–C–O isotope geochemistry of the Bultfontein kimberlite (Kimberley, South Africa). *Chemical Geology* **455**, 342–356.

Graham, S., Lambert, D. & Shee, S. (2004). The petrogenesis of carbonatite, melnoite and kimberlite from the Eastern Goldfields Province, Yilgarn Craton. *Lithos* **76**, 519–533.

Guarino, V., Wu, F.-Y., Lustrino, M., Melluso, L., Brotzu, P., Gomes, C. D. B., Ruberti, E., Tassinari, C. C. G. & Svisero, D. P. (2013). U–Pb ages, Sr–Nd-isotope geochemistry, and petrogenesis of kimberlites, kamafugites and phlogopite-picrites of the Alto Paranaíba Igneous Province, Brazil. *Chemical Geology* **353**, 65–82.

Guo, J. & Green, T. H. (1990). Experimental study of barium partitioning between phlogopite and silicate liquid at upper-mantle pressure and temperature. *Lithos* **24**, 83–95.

Holten, T., Jamtveit, B. & Meakin, P. (2000). Noise and oscillatory zoning of minerals. *Geochimica et Cosmochimica Acta* **64**, 1893–1904.

Hutchison, M. T. & Frei, D. (2009). Kimberlite and related rocks from Garnet Lake, West Greenland, including their mantle constituents, diamond occurrence, age and provenance. *Lithos* **112**, 318–333.

Jelsma, H., Barnett, W., Richards, S. & Lister, G. (2009). Tectonic setting of kimberlites. *Lithos* **112**, 155–165.

Jelsma, H. A., De Wit, M. J., Thiart, C., Dirks, P. H. G. M., Viola, G., Basson, I. J. & Anckar, E. (2004). Preferential distribution along transcontinental corridors of kimberlites and related rocks of Southern Africa. *South African Journal of Geology* **107**, 301–324.

Kamber, B. S., Greig, A., Schoenberg, R. & Collerson, K. D. (2003). A refined solution to Earth's hidden niobium: implications for evolution of continental crust and mode of core formation. *Precambrian Research* **126**, 289–308.

Kargin, A. V., Nosova, A. A., Larionova, Y. O., Kononova, V. A., Borisovsky, S. E., Koval'chuk, E. V. & Griboedova, I. G. (2014). Mesoproterozoic orangeites (Kimberlites II) of West Karelia: Mineralogy, geochemistry, and Sr–Nd isotope composition. *Petrology* **22**, 151–183.

Kjarsgaard, B. A., Pearson, D. G., Tappe, S., Nowell, G. M. & Dowall, D. P. (2009). Geochemistry of hypabyssal kimberlites from Lac de Gras, Canada: Comparisons to a global database and applications to the parent magma problem. *Lithos* **112**, 236–248.

Kopylova, M. G., Mogg, T. & Smith, B. S. (2010). Mineralogy of the Snap Lake kimberlite, Northwest Territories, Canada, and compositions of phlogopite as records of its crystallization. *Canadian Mineralogist* **48**, 549–570.

Kramm, U., Kogarko, L. N., Kononova, V. A. & Vartiainen, H. (1993). The Kola Alkaline Province of the CIS and Finland: Precise Rb–Sr ages define 380–360 Ma age range for all magmatism. *Lithos* **30**, 33–44.

Laajoki, K. (2005). Karelian supracrustal rocks. In: Lehtinen, M., Nurmi, P. A. & Rämö, O. T. (eds) *Precambrian Geology of Finland—Key to the Evolution of the Fennoscandian Shield*. Amsterdam: Elsevier, pp. 279–341.

Larionova, Y. O., Sazonova, L. V., Lebedeva, N. M., Nosova, A. A., Tretyachenko, V. V., Travin, A. V., Kargin, A. V. & Yudin, D. S. (2016). Kimberlite age in the Arkhangelsk Province, Russia: isotopic geochronologic Rb–Sr and $^{40}Ar/^{39}Ar$ and mineralogical data on phlogopite. *Petrology* **24**, 562–593.

Larsen, L. M., Heaman, L. M., Creaser, R. A., Duncan, R. A., Frei, R. & Hutchison, M. (2009). Tectonomagmatic events during stretching and basin formation in the Labrador Sea and the Davis Strait: evidence from age and composition of Mesozoic to Palaeogene dyke swarms in West Greenland. *Journal of the Geological Society, London* **166**, 999–1012.

Lee, M.-J., Lee, J.-I., Jaques, M. & Kim, Y. (2003). Petrography and geochemistry of the Devonian ultramafic lamprophyre at Sokli in the northeastern Baltic Shield (Finland). *Journal of the Petrological Society of Korea* **12**, 170–183.

Lee, M. J., Lee, J. I. & Moutte, J. (2005). Compositional variation of Fe−Ti oxides from the Sokli complex, northeastern Finland. *Geosciences Journal* **9**, 1–13.

Lehtonen, M. & O'Brien, H. (2009). Mantle transect of the Karelian Craton from margin to core based on *PT* data from garnet and clinopyroxene xenocrysts in kimberlites. *Bulletin of the Geological Society of Finland* **81**, 79–102.

le Roex, A. P. (1986). Geochemical correlation between southern African kimberlites and South Atlantic hotspots. *Nature* **324**, 243–245.

le Roex, A. P., Bell, D. R. & Davis, P. (2003). Petrogenesis of group I kimberlites from Kimberley, South Africa: evidence from bulk-rock geochemistry. *Journal of Petrology* **44**, 2261–2286.

Liu, Y. & Comodi, P. (1993). Some aspects of the crystal-chemistry of apatites. *Mineralogical Magazine* **57**, 709–720.

Locock, A. J. & Mitchell, R. H. (2018). Perovskite classification: An Excel spreadsheet to determine and depict end-member proportions for the perovskite- and vapnikite-subgroups of the perovskite supergroup. *Computers & Geosciences* **113**, 106–114.

Ludwig, K. R. (2003). *Isoplot 3.00: a geochronological toolkit for Microsoft Excel. Berkeley Geochronology Center*, Special Publication **4**, 70 pp.

Maas, R., Grew, E. S. & Carson, C. J. (2015). Isotopic constraints (Pb, Rb–Sr, Sm–Nd) on the sources of early Cambrian pegmatites with boron and beryllium minerals in the Larsemann Hills, Prydz Bay, Antarctica. *Canadian Mineralogist* **53**, 249–272.

Mahotkin, I. L., Gibson, S. A., Thompson, R. N., Zhuravlev, D. Z. & Zherdev, P. U. (2000). Late Devonian diamondiferous kimberlite and alkaline picrite (proto-kimberlite?) magmatism in the Arkhangelsk Region, NW Russia. *Journal of Petrology* **41**, 201–227.

Martins, T., Chakhmouradian, A. R. & Medici, L. (2014). Perovskite alteration in kimberlites and carbonatites: the role of Kassite, $CaTi_2O_4(OH)_2$. *Physics and Chemistry of Minerals* **41**, 473–484.

Mitchell, R. H. (1979). The alleged kimberlite–carbonatite relationship; additional contrary mineralogical evidence. *American Journal of Science* **279**, 570–589.

Mitchell, R. H. (1986). *Kimberlites: Mineralogy, Geochemistry, and Petrology*. New York: Springer Science & Business Media.

Mitchell, R. H. (1995). *Kimberlites, Orangeites, and Related Rocks*. New York: Springer Science & Business Media.

Mitchell, R. H. (2008). Petrology of hypabyssal kimberlites: Relevance to primary magma compositions. *Journal of Volcanology and Geothermal Research* **174**, 1–8.

Mitchell, R. H. (2013). Paragenesis and oxygen isotopic studies of serpentine in kimberlite. In: Pearson, D. G. Grütter, H. S. Harris, J. W. Kjarsgaard, B. A. O'Brien, H. Rao, N.V.C. & Sparks, S. (eds) *Proceedings of 10th International Kimberlite Conference*. Berlin: Springer, pp. 1–12.

Mitchell, R. H. & Bergman, S. C. (1991). *Petrology of Lamproites*. Berlin: Springer.

Mogg, T., Kopylova, M., Scott Smith, B. & Kirkley, M. (2003). Petrology of the Snap Lake kimberlite, NWT, Canada. In: *8th International Kimberlite Conference, Victoria, Canada, Extended Abstracts*, p. 5.

Nielsen, T. F. D., Jensen, S. M., Secher, K. & Sand, K. K. (2009). Distribution of kimberlite and aillikite in the Diamond Province of southern West Greenland: a regional perspective based on groundmass mineral chemistry and bulk compositions. *Lithos* **112**, 358–371.

Nironen, M. (2017). Guide to the geological map of Finland—BEDROCK 1:1000000. *Geological Survey of Finland, Special Paper* **60**, 41–76.

Nowell, G. M., Pearson, D. G., Bell, D. R., Carlson, R. W., Smith, C. B., Kempton, P. D. & Noble, S. R. (2004). HF isotope systematics of kimberlites and their megacrysts: new constraints on their source regions. *Journal of Petrology* **45**, 1583–1612.

O'Brien, H. (2015). Kimberlite-hosted diamonds in Finland. In: Maier, W. D., Lahtinen, R. & O'Brien, H. (eds) *Mineral Deposits of Finland*. New York: Elsevier, pp. 345–375.

O'Brien, H. E. & Bradley, J. (2008). New kimberlite discoveries in Kuusamo, Northern Finland. In: 9th International Kimberlite Conference, Frankfurt, Germany, Extended Abstracts, p. 3.

O'Brien, H. & Hyvönen, E. (2015). The Sokli carbonatite complex. In: Maier, W. D., Lahtinen, R. & O'Brien, H. (eds) *Mineral Deposits of Finland*. New York: Elsevier, pp. 305–325.

O'Brien, H. & Lehtonen, M. (2012). Craton mantle formation and structure of Eastern Finland Mantle: evidence from kimberlite-derived mantle xenoliths, xenocrysts and diamonds. In: Haapala, I. (ed) *From the Earth's Core to Outer Space*. Berlin: Springer, pp. 61–80.

O'Brien, H. E. & Tyni, M. (1999). Mineralogy and geochemistry of kimberlites and related rocks from Finland. In: Gurney, J. J., Gurney, J. L., Pascoe, M. D. & Richardson, S. H. (eds) *Proceedings of the 7th International Kimberlite Conference*. Cape Town: Red Roof Design, pp. 625–636.

O'Brien, H. E., Peltonen, P. & Vartiainen, H. (2005). Kimberlites, carbonatites, and alkaline rocks. In: Lehtinen, M., Nurmi, P. A. & Rämö, O. T. (eds) *Precambrian Geology of Finland—Key to the Evolution of the Fennoscandian Shield*. Amsterdam: Elsevier, pp. 605–644.

O'Brien, H., Phillips, D. & Spencer, R. (2007). Isotopic ages of Lentiira–Kuhmo–Kostomuksha olivine lamproite–Group II kimberlites. *Bulletin of the Geological Society of Finland* **79**, 203.

Odin, G. S. (1982). *Numerical Dating in Stratigraphy*. New York: John Wiley.

Pan, Y. & Fleet, M. E. (2002). Compositions of the apatite-group minerals: substitution mechanisms and controlling factors. In: Kohn, M. J., Rakovan, J. & Hughes, J. M. (eds) *Phosphates: Geochemical, Geobiological and Materials Importance. Mineralogical Society of America and Geochemical Society, Reviews in Mineralogy and Geochemistry* **48**, 13–49.

Parrish, J. B. & Lavin, P. M. (1982). Tectonic model for kimberlite emplacement in the Appalachian Plateau of Pennsylvania. *Geology* **10**, 344–347.

Peltonen, P., Mänttäri, I., Huhma, H. & Whitehouse, M. J. (2006). Multi-stage origin of the lower crust of the Karelian craton from 3.5 to 1.7 Ga based on isotopic ages of kimberlite-derived mafic granulite xenoliths. *Precambrian Research* **147**, 107–123.

Peng, G., Luhr, J. F. & McGee, J. J. (1997). Factors controlling sulfur concentrations in volcanic apatite. *American Mineralogist* **82**, 1210–1224.

Phillips, D., Machin, K. J., Kiviets, G. B., Fourie, L. F., Roberts, M. A. & Skinner, E. M. W. (1998). A petrographic and $^{40}Ar/^{39}Ar$ geochronological study of the Voorspoed Kimberlite, South Africa: Implications for the origin of Group II Kimberlite magmatism. *South African Journal of Geology* **101**, 299.

Phillips, D., Matchan, E. L., Honda, M. & Kuiper, K. F. (2017a). Astronomical calibration of $^{40}Ar/^{39}Ar$ reference minerals using high-precision, multi-collector (ARGUSVI) mass spectrometry. *Geochimica et Cosmochimica Acta* **196**, 351–369.

Phillips, D., Zhong, D., Matchan, E. L., Maas, R., Farr, H., O'Brien, H. & Giuliani, A. (2017b). A comparison of geochronology methods applied to kimberlites and related rocks from the Karelian Craton, Finland. In: *11th International Kimberlite Conference, Gaborone, Botswana, Extended Abstracts, p. 3*.

Pouchou, J. & Pichoir, F. (1984). A new model for quantitative X-ray microanalysis. I.—Application to the analysis of homogeneous samples. *Recherche Aérospatiale* **3**, 167–192.

Reguir, E. P., Chakhmouradian, A. R., Halden, N. M., Malkovets, V. G. & Yang, P. (2009). Major- and trace-element compositional variation of phlogopite from kimberlites and carbonatites as a petrogenetic indicator. *Lithos* **112**, 372–384.

Righter, K. & Carmichael, I. S. E. (1996). Phase equilibria of phlogopite lamprophyres from western Mexico: biotite–liquid equilibria and *P–T* estimates for biotite-bearing igneous rocks. *Contributions to Mineralogy and Petrology* **123**, 1–21.

Rock, N. M. S. (1986). The nature and origin of ultramafic lamprophyres: alnöites and allied rocks. *Journal of Petrology* **27**, 155–196.

Rock, N. M. S. (1987). The nature and origin of lamprophyres: an overview. In: Fitton, J. G. & Upton, B. G. J. (eds) *Alkaline Igneous Rocks. Geological Society, London, Special Publications* **30**, 191–226.

Rock, N. M. S. (1991). *Lamprophyres*. Glasgow: Blackie; New York: Van Nostrand Reinhold.

Roeder, P. L. & Schulze, D. J. (2008). Crystallization of groundmass spinel in kimberlite. *Journal of Petrology* **49**, 1473–1495.

Rouse, R. C. & Dunn, P. J. (1982). A contribution to the crystal chemistry of ellestadite and the silicate sulfate apatites. *American Mineralogist* **67**, 90–96.

Rudnick, R. L. & Fountain, D. M. (1995). Nature and composition of the continental crust: a lower crustal perspective. *Reviews of Geophysics* **33**, 267–309.

Sarkar, C., Kjarsgaard, B. A., Pearson, D. G., Heaman, L. M., Locock, A. J. & Armstrong, J. P. (2018). Geochronology, classification and mantle source characteristics of kimberlites and related rocks from the Rae Craton, Melville Peninsula, Nunavut, Canada. *Mineralogy and Petrology* **112**, 653–672.

Scott-Smith, B. H., Danchin, R., Harris, J. & Stracke, K. (1984). Kimberlites near Orroroo, South Australia. In: Kornprobst, J. (ed.) *Kimberlites I: Kimberlites and Related Rocks*. Amsterdam: Elsevier, pp. 121–142.

Scott Smith, B., Nowicki, T., Russell, J., Webb, K., Mitchell, R., Hetman, C., Harder, M., Skinner, E. & Robey, J. A. (2013). Kimberlite terminology and classification. In: Pearson, D. G. Grütter, H. S. Harris, J. W. Kjarsgaard, B. A. O'Brien, H. Rao, N.V.C. & Sparks, S. (eds) *Proceedings of 10th International Kimberlite Conference*. Berlin: Springer, pp. 1–17.

Secher, K., Heaman, L. M., Nielsen, T. F. D., Jensen, S. M., Schjøth, F. & Creaser, R. A. (2009). Timing of kimberlite, carbonatite, and ultramafic lamprophyre emplacement in the alkaline province located 64°–67° N in southern West Greenland. *Lithos* **112**, 400–406.

Seifert, W., Kämpf, H. & Wasternack, J. (2000). Compositional variation in apatite, phlogopite and other accessory minerals of the ultramafic Delitzsch complex, Germany: implication for cooling history of carbonatites. *Lithos* **53**, 81–100.

Shaikh, A. M., Patel, S. C., Ravi, S., Behera, D. & Pruseth, K. L. (2017). Mineralogy of the TK1 and TK4 'kimberlites' in the Timmasamudram cluster, Wajrakarur Kimberlite Field, India: Implications for lamproite magmatism in a field of kimberlites and ultramafic lamprophyres. *Chemical Geology* **455**, 208–230.

Shaikh, A. M., Kumar, S. P., Patel, S. C., Thakur, S. S., Ravi, S. & Behera, D. (2018). The P3 kimberlite and P4 lamproite, Wajrakarur kimberlite field, India: mineralogy, and major and minor element compositions of olivines as records of their phenocrystic vs xenocrystic origin. *Mineralogy and Petrology* **112**, 609–624.

Shee, S., Clement, C. & Skinner, E. (1994). The petrology of the Wesselton kimberlite sills, Kimberley, Cape Province, South Africa. In: Meyer, H. O. A. & Leonardos, O. H. (eds) *Kimberlites, Related Rocks and Mantle Xenoliths*.

Proceedings of the 5th International Kimberlite Conference. Rio de Janeiro, Brasil: CPRM, pp. 98–114.

Shore, M. & Fowler, A. D. (1996). Oscillatory zoning in minerals; a common phenomenon. *Canadian Mineralogist* **34**, 1111–1126.

Skinner, E. (1989). Contrasting Group I and Group II kimberlite petrology: towards a genetic model for kimberlites. In: Glover, J. & Harris, P. (eds) *Kimberlites and Related Rocks, 4th International Kimberlite Conference*. Perth, Australia: Geological Society of Australia, pp. 528–544.

Skinner, E. M. W., Smith, C. B., Viljoen, K. S. & Clark, T. C. (1994). The petrography, tectonic setting and emplacement ages of kimberlites in the southwestern border region of the Kaapvaal craton, Prieska area. In: Meyer, H. O. A. & Leonardos, O. H. (eds) *Kimberlites, Related Rocks and Mantle Xenoliths. Proceedings of the 5th International Kimberlite Conference. Rio de Janeiro, Brasil: CPRM*, pp. 80–97.

Slabunov, A. I., Lobach-Zhuchenko, S. B., Bibikova, E. V., Balagansky, V. V., Sorjonen-Ward, P., Volodichev, O. I., Shchipansky, A. A., Svetov, S. A., Chekulaev, V. P., Arestova, N. A. & Stepanov, V. S. (2006). The Archean of the Baltic Shield: geology, geochronology, and geodynamic settings. *Geotectonics* **40**, 409–433.

Smart, K. A., Cartigny, P., Tappe, S., O'Brien, H. & Klemme, S. (2017). Lithospheric diamond formation as a consequence of methane-rich volatile flooding: An example from diamondiferous eclogite xenoliths of the Karelian craton (Finland). *Geochimica et Cosmochimica Acta* **206**, 312–342.

Smith, C. B. (1983). Pb, Sr and Nd isotopic evidence for sources of southern African Cretaceous kimberlites. *Nature* **304**, 51–54.

Smith, C. B., Gurney, J., Ebrahim, N., Skinner, E. & Clement, C. (1985). Geochemical character of southern African kimberlites: a new approach based on isotopic constraints. *Transactions of the Geological Society of South Africa* **88**, 267–280.

Smith, C. B., Haggerty, S. E., Chatterjee, B., Beard, A. & Townend, R. (2013). Kimberlite, lamproite, ultramafic lamprophyre, and carbonatite relationships on the Dharwar Craton, India; an example from the Khaderpet pipe, a diamondiferous ultramafic with associated carbonatite intrusion. *Lithos* **182**, 102–113.

Soltys, A., Giuliani, A. & Phillips, D. (2018). A new approach to reconstructing the composition and evolution of kimberlite melts: a case study of the archetypal Bultfontein kimberlite (Kimberley, South Africa). *Lithos* **304–307**, 1–15.

Sommerauer, J. & Katz-Lehnert, K. (1985). A new partial substitution mechanism of CO_3^{2-}/CO_3OH^{3-} and SiO_4^{4-} for the PO_4^{3-} group in hydroxyapatite from the Kaiserstuhl alkaline complex (SW-Germany). *Contributions to Mineralogy and Petrology* **91**, 360–368.

Sorjonen-Ward, P. & Luukkonen, E. J. (2005). Archean rocks. In: Lehtinen, M., Nurmi, P. A. & Rämö, O. T. (eds) *Precambrian Geology of Finland—Key to the Evolution of the Fennoscandian Shield*. Amsterdam: Elsevier, pp. 19–99.

Sparks, R. S. J. (2013). Kimberlite volcanism. *Annual Review of Earth and Planetary Sciences* **41**, 497–528.

Stripp, G. R., Field, M., Schumacher, J. C., Sparks, R. S. J. & Cressey, G. (2006). Post-emplacement serpentinization and related hydrothermal metamorphism in a kimberlite from Venetia, South Africa. *Journal of Metamorphic Geology* **24**, 515–534.

Sun, J., Liu, C.-Z., Tappe, S., Kostrovitsky, S. I., Wu, F.-Y., Yakovlev, D., Yang, Y.-H. & Yang, J.-H. (2014). Repeated kimberlite magmatism beneath Yakutia and its relationship to Siberian flood volcanism: Insights from *in situ* U–Pb and Sr–Nd perovskite isotope analysis. *Earth and Planetary Science Letters* **404**, 283–295.

Sun, S-S. & McDonough, W. F. (1989). Chemical and isotopic systematics of oceanic basalts: implications for mantle composition and processes. In: Saunders, A. D. & Norry, M. J. (eds) *Magmatism in the Ocean Basins. Geological Society, London, Special Publications* **42**, 313–345.

Sunrise Diamonds PLC (2010). Submission Report SCD 45 & 47 claim, p. 10. Cheshire, United Kingdom 2010 report: http://tupa.gtk.fi/raportti/valtaus/8017_2_1.pdf.

Sunrise Diamonds PLC (2014). Relinquishment Report SCD199, p. 54. Cheshire, United Kingdom 2014 report: http://tupa.gtk.fi/raportti/valtaus/7996_2.pdf.

Tappe, S., Steenfelt, A., Heaman, L. M. & Simonetti, A. (2009). The newly discovered Jurassic Tikiusaaq carbonatite-aillikite occurrence, West Greenland, and some remarks on carbonatite–kimberlite relationships. Lithos **112**, 385–399.

Tappe, S., Jenner, G. A., Foley, S. F., Heaman, L., Besserer, D., Kjarsgaard, B. A. & Ryan, B. (2004). Torngat ultramafic lamprophyres and their relation to the North Atlantic Alkaline Province. *Lithos* **76**, 491–518.

Tappe, S., Foley, S. F., Jenner, G. A. & Kjarsgaard, B. A. (2005). Integrating ultramafic lamprophyres into the IUGS classification of igneous rocks: rationale and implications. *Journal of Petrology* **46**, 1893–1900.

Tappe, S., Foley, S. F., Jenner, G. A., Heaman, L. M., Kjarsgaard, B. A., Romer, R. L., Stracke, A., Joyce, N. & Hoefs, J. (2006). Genesis of ultramafic lamprophyres and carbonatites at Aillik Bay, Labrador: a consequence of incipient lithospheric thinning beneath the North Atlantic Craton. *Journal of Petrology* **47**, 1261–1315.

Tappe, S., Foley, S. F., Stracke, A., Romer, R. L., Kjarsgaard, B. A., Heaman, L. M. & Joyce, N. (2007). Craton reactivation on the Labrador Sea margins: $^{40}Ar/^{39}Ar$ age and Sr–Nd–Hf–Pb isotope constraints from alkaline and carbonatite intrusives. *Earth and Planetary Science Letters* **256**, 433–454.

Tappe, S., Foley, S. F., Kjarsgaard, B. A., Romer, R. L., Heaman, L. M., Stracke, A. & Jenner, G. A. (2008). Between carbonatite and lamproite—diamondiferous Torngat ultramafic lamprophyres formed by carbonate-fluxed melting of cratonic MARID-type metasomes. *Geochimica et Cosmochimica Acta* **72**, 3258–3286.

Tappe, S., Pearson, D. G., Nowell, G., Nielsen, T., Milstead, P. & Muehlenbachs, K. (2011). A fresh isotopic look at Greenland kimberlites: Cratonic mantle lithosphere imprint on deep source signal. *Earth and Planetary Science Letters* **305**, 235–248.

Tappe, S., Graham Pearson, D., Kjarsgaard, B. A., Nowell, G. & Dowall, D. (2013). Mantle transition zone input to kimberlite magmatism near a subduction zone: Origin of anomalous Nd–Hf isotope systematics at Lac de Gras, Canada. *Earth and Planetary Science Letters* **371–372**, 235–251.

Tappe, S., Kjarsgaard, B. A., Kurszlaukis, S., Nowell, G. M. & Phillips, D. (2014). Petrology and Nd–Hf isotope geochemistry of the Neoproterozoic Amon Kimberlite Sills, Baffin Island (Canada): evidence for deep mantle magmatic activity linked to supercontinent cycles. *Journal of Petrology* **55**, 2003–2042.

Tappe, S., Brand, N. B., Stracke, A., van Acken, D., Liu, C.-Z., Strauss, H., Wu, F.-Y., Luguet, A. & Mitchell, R. H. (2017a). Plates or plumes in the origin of kimberlites: U/Pb perovskite and Sr–Nd–Hf–Os–C–O isotope constraints from the Superior craton (Canada). *Chemical Geology* **455**, 57–83.

Tappe, S., Romer, R. L., Stracke, A., Steenfelt, A., Smart, K. A., Muehlenbachs, K. & Torsvik, T. H. (2017b). Sources and mobility of carbonate melts beneath cratons, with implications

for deep carbon cycling, metasomatism and rift initiation. *Earth and Planetary Science Letters* **466**, 152–167.

Tappe, S., Smart, K., Torsvik, T., Massuyeau, M. & de Wit, M. (2018). Geodynamics of kimberlites on a cooling Earth: clues to plate tectonic evolution and deep volatile cycles. *Earth and Planetary Science Letters* **484**, 1–14.

Tompkins, L. (1999). Petrology and geochemistry of kimberlite from Shandong and Lianing provinces, China. In: Gurney, J. J., Gurney, J. L., Pascoe, M. D. and Richardson, S. H. (eds) *Proceedings of the 7th International Kimberlite Conference*. Cape Town: Red Roof Design, pp. 872–887.

Vartiainen, H., Kresten, P. & Kafkas, Y. (1978). Alkaline lamprophyres from the Sokli Complex, northern Finland. *Bulletin of the Geological Society of Finland* **50**, 59–68.

Villa, I. M., De Bièvre, P., Holden, N. E. & Renne, P. R. (2015). IUPAC–IUGS recommendation on the half life of ^{87}Rb. *Geochimica et Cosmochimica Acta* **164**, 382–385.

Wang, L.-X., Marks, M. A. W., Wenzel, T., Von Der Handt, A., Keller, J., Teiber, H. & Markl, G. (2014). Apatites from the Kaiserstuhl Volcanic Complex, Germany: new constraints on the relationship between carbonatite and associated silicate rocks. *European Journal of Mineralogy* **26**, 397–414.

White, J., Sparks, R., Bailey, K., Barnett, W., Field, M. & Windsor, L. (2012). Kimberlite sills and dykes associated with the Wesselton kimberlite pipe, Kimberley, South Africa. *South African Journal of Geology* **115**, 1–32.

White, S. H., de Boorder, H. & Smith, C. B. (1995). Structural controls of kimberlite and lamproite emplacement. *Journal of Geochemical Exploration* **53**, 245–264.

Williams, H. R. & Williams, R. A. (1977). Kimberlites and plate-tectonics in West Africa. *Nature* **270**, 507–508.

Woodhead, J., Hergt, J., Giuliani, A., Phillips, D. & Maas, R. (2017). Tracking continental-scale modification of the Earth's mantle using zircon megacrysts. *Geochemical Perspectives Letters* **4**, 1–6.

Woolley, A. R., Bergman, S. C., Edgar, A. D., Le Bas, M. J., Mitchell, R. H., Rock, N. M. & Smith, B. H. S. (1996). Classification of lamprophyres, lamproites, kimberlites, and the kalsilitic, melilitic, and leucitic rocks. *Canadian Mineralogist* **34**, 175–186.

Wyatt, B. A., Baumgartner, M., Anckar, E. & Grutter, H. (2004). Compositional classification of 'kimberlitic' and 'non-kimberlitic' ilmenite. *Lithos* **77**, 819–840.

Yaxley, G. M., Kamenetsky, V. S., Nichols, G. T., Maas, R., Belousova, E., Rosenthal, A. & Norman, M. (2013). The discovery of kimberlites in Antarctica extends the vast Gondwanan Cretaceous province. *Nature Communications* **4**, 2921.